Numerical Simulation of a Midlatitude Squall Line in Two Dimensions

ROBERT G. FOVELL AND YOSHI OGURA

Department of Atmospheric Sciences, University of Illinois, Urbana, Illinois

(Manuscript received 22 December 1987, in final form 13 July 1988)

ABSTRACT

A two-dimensional, anelastic cloud model was used in attempts to numerically replicate the observed structure of a midlatitude squall line. Initial conditions were adapted from observations of the 22 May 1976 Oklahoma line. Model simulations were made with and without considering the ice phase of water. These model storms have, within the constraints of the model's geometry, replicated the basic multicellular character and general line-normal airflow typical of these lines. In addition, the structure and intensity of the subcloud cold air pool and the propagation speeds developed by the storms appear to be reasonable.

Further, it was found that the initial conditions chosen resulted in model storms which were not only long-lasting but also essentially repetitive, indicating that a state of quasi-equilibrium had been attained. The storms did not decay because the environmental conditions ahead of the storms were favorable and essentially unchanged during the course of the simulations.

The inclusion of ice phase processes resulted in the production of more realistic appearing features in the trailing portion of the storm as well as more widespread precipitation. These were for the most part due to the enhanced rearward transport of precipitation particles from the convective cells which resulted from including ice, particularly low density snow. The underlying structures of these model storms were investigated by averaging model fields across time, smoothing out the transient components. These analyses indicated that the addition of ice had its greatest impact on the scale of the storm's circulation features.

1. Introduction

This paper reports on attempts to replicate the convective and mesoscale structure of a midlatitude, multicellular squall line. While many field observations of multicellular storms have been made over the last few decades, among them the important works of Newton (1950, 1966) and Zipser (1969), recent studies, including those of Ogura and Liou [1980 (OL)], Smull and Houze [1985 (SH1); 1987a (SH2); 1987b (SH3)], and Heymsfield and Schotz (1985), have provided information about the line-normal structure of midlatitude systems in detail sufficient to be usable for verification of numerical simulations. These studies have focused on cloud- and/or mesoscale airflow and transports of quantities such as mass, moisture and momentum through their storms. In addition, analyses of multicellular convective systems which passed through the National Hail Research Experiment (NHRE) mesonetwork by Fankhauser (1982), Foote and Wade (1982) and others have provided data on the evolution of individual cells and precipitation formation processes. Observations of tropical systems which complement these midlatitude studies include Zipser (1977), Gamache and Houze (1982, 1983, 1985), Roux et al. (1984) and Chong et al. (1987), among many others.

In particular, Smull and Houze (1987a), using single- and dual-Doppler radar data, have presented a conceptual model of the line-normal structure of a midlatitude squall line, the 22 May 1976 storm also studied by Ogura and Liou (1980) and Smull and Houze (1985, 1987b). Their model is reproduced here in Fig. 1. In broad terms, the system-relative airflow within the storm consisted of environmental air, ingested at low levels from ahead of the storm and accelerated over the cold subcloud outflow which was produced by evaporative cooling of precipitation particles. The line itself was generally oriented perpendicular to the vertical wind shear vector and the rising front-to-rear airflow jet gave the storm a system-relative circulation tilted with height in the upshear direction. Embedded within this airflow were areas where the updraft was particularly concentrated—in the convective cells. A typical cell became identifiable as a local radar reflectivity maximum at the front of the storm (first echo) at a height of about 5 km. It intensified as it moved rearward, increased in vertical extent and induced downdrafts at high levels where outflow from cell tops converged with environmental inflow and forward-directed outflow from older cells. Low-level downdrafts produced by precipitation loading and evaporative cooling developed beneath the mature cells. SH1 found that individual cells in this storm translated with an

Corresponding author address: Dr. Robert G. Fovell, Dept. of Atmospheric Sciences, AK-40, University of Washington, Seattle, WA 98195.

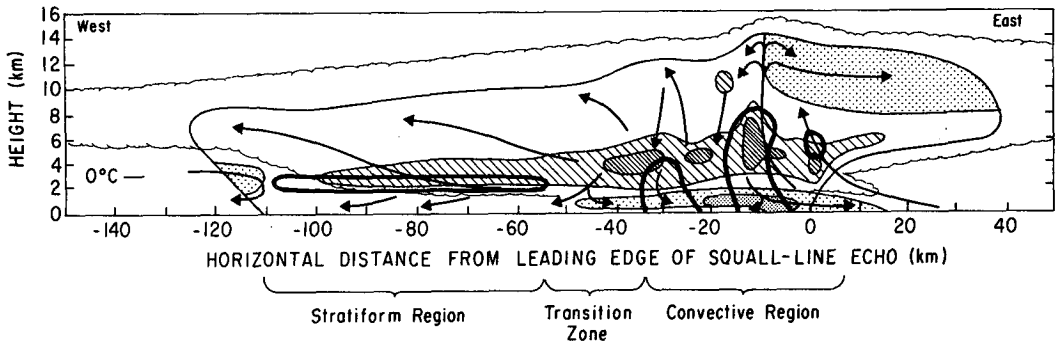

FIG. 1. Smull and Houze's (1987a) conceptual model of the circulation during the mature phase of the 22 May 1976 squall line, which is described in detail in that paper. System motion is from left to right at 15 m s^{-1}. System-relative airflow is generally right to left (towards the rear) except where stippled; hatched areas show where rearward flow is stronger. Outermost solid line denotes boundary of detectable radar echo; heavy solid lines enclose more intense features.

eastward component of about 6 m s^{-1} while the line moved at a speed of 15 m s^{-1} in the same direction so that in a system-relative sense the cells were moving rapidly toward the rear of the storm.

The aging cell died when a new cell appeared ahead of it over the outflow, grew and cut off the older cell's source of moisture. As it decayed its echo top descended towards the melting level. Each cell lived sufficiently long that a cross section taken perpendicular to the line would show a number of cells in various stages of their evolution as in the composite.

At the rear of the system, a horizontally extensive maximum of radar reflectivity was found, located near the melting level. This was the so-called "bright band" which has been observed in the trailing regions of many midlatitude and tropical squall lines. The physical location of these bands, with respect to the horizontal and vertical, can be partially explained by the melting of low density ice particles (snow) which, in their completely frozen state, reflect radar waves much more poorly than raindrops. However, as they melt, they acquire a coating of liquid water which creates localized improvement in reflectivity. In addition, these ice particles can aggregate as they descend and thus increase in both size and density, thereby presenting larger, better reflecting targets for the radar (e.g., Stewart et al. 1984).

The storm structure in the bright band region was horizontally rather uniform and stratified, contrasting with the far less uniform appearance of the active convection portion of the storm near the leading edge. Between these regions SH2 detected a zone, characterized at low levels by a minimum in reflectivity and a local maximum in mesoscale descending motion, which they termed the transition region. Throughout the storm, rearward flow was found to be maximized in a layer centered at about 4 km above ground level (AGL) with superimposed perturbations associated with the convective cells. Qualitatively similar structures have been found in many other squall line studies.

Also at the rear, SH2 found that dry air from the postsquall environment was intruding into the system. In this case, this intrusion did not reach as far forward into the storm as it did in two other cases examined by them in another study (SH3). In that paper, two lines in which the rear inflow penetrated all the way into the active convection region were analyzed. They reasoned that this inflow was induced in response to the storm itself and did not represent a current of air from the post-squall environment overtaking the storm. Also, they presented evidence that the rear inflow observed in the 22 May case was becoming more established with time.

The simulations presented herein represent attempts to replicate the basic elements of the Smull–Houze conceptual model with a two-dimensional (2D), anelastic cloud model. In the process, we hope to gain a better understanding of the physical processes involved in maintaining a long-lived squall line. One might wonder, however, whether the essential characteristics of this conceptual structure can be captured in a 2D model. In the Oklahoma squall lines examined by Bluestein and Jain (1985), the largest component of the individual cell's motion was found to be along the line with only a small component rearward. This raises the possibility that flow between cells along the line is important. Zipser (1969) clearly demonstrated that potentially cold air from the midtroposphere ahead of the storm can pass between the individual cells along the line, feed into the downdrafts and enter the subcloud zone, something that cannot directly occur in a two-dimensional model. However, the fact that variation in storm structure is much greater for a given distance normal to the line than along it has been used in the past as the principle justification for two-dimensional modeling.

Previous 2D modeling studies have resulted in simulated circulation features which appear to be relatively realistic when compared to the observations. Thorpe et al. [1982 (TMM)], for example, was able to produce

a long-lived, apparently unicellular storm. This storm resulted when the vertical wind shear was confined to the lowest 2.5 km. When wind profiles containing shear through a deeper layer were employed, the resulting storms were considerably weaker and not long-lived.

A quasi-2D West African squall line was numerically replicated by Dudhia et al. [1987 (DMS)]. Their model storm was also long-lived, lasting over 10 h, and exhibited obvious multicellular behavior. They found the period of cellular development to be between 30 and 40 min and cell separation distances were between 15 and 20 km. An interesting result of their simulation is that weaker cells tended to alternate with stronger cells. The circulation in the cold outflow at the leading edge was not explicitly addressed by SH1 and SH2 but it is likely that it would agree with the rotor, jump downdraft and overturning downdraft model of DMS and earlier, related studies.

In DMS, a multicellular storm was created only when the environmental wind profile (in a system-relative sense) contained a large, rearward-directed jet in the cloud layer. When this jet was removed, a unicell storm resulted. The failure of the unicell simulation to exhibit multicellular character was explained by the absence of winds to force the cell rearward. Note, however, that typical midlatitude multicellular storms produce downstream propagating cells even in the face of unidirectional shear. This point needs to be investigated.

Klemp et al. [1985 (KRW)] used a 2D model initialized with environmental conditions typical of the midlatitudes and found the resulting model storm to evolve through three stages during the course of the simulation. They termed the first the "initial phase"; the circulation during this time was dominated by the forcing used to initiate the convection. Later, the storm was found to go through a "periodically redeveloping phase" during which the storm updraft oscillated between system-relative vertical and downshear tilted orientations with height. KRW found that the length of time the storm spend in this phase was a function of wind shear; environments with smaller shear allowed the storm to organize more quickly.

The final stage was called the "surging out phase" and was marked by the onset of system-relative upshear tilt in the storm's updraft circulation. In a later work, Rotunno, Klemp and Weisman [1988 (RKW)] argued that the generally weaker updrafts produced during this stage reflect a state of imbalance between the positive vorticity associated with the vertical wind shear and the negative vorticity generated by the subcloud cold pool. This state, while it may be "less-than-optimal" with respect to its ability to produce deep vertical lifting, is nonetheless associated with an effective updraft orientation (Browning 1977). Precipitation produced within the tilting updraft falls in such a way as it neither erodes the updraft nor alters the convective instability of the environmental air feeding it at low levels. Indeed, the cold pool, established through the evaporation of this precipitation, is known to play an important role in the generation of new convective elements which, under the proper conditions, give the storm its multicellular character.

We might also ask how important is the mesoscale pressure gradient aloft in the momentum budget normal to a sqall line. Using aircraft measurements taken in tropical convective bands, LeMone (1983) and LeMone et al. (1984) identified mesoscale regions of low pressure located behind thelines and centered above the ground. Their pressure fields were found to be hydrostatic to a large degree. However, they also noted the importance of dynamic (nonhydrostatic) pressure effects. Since pressure fields are not easily estimated from rawinsonde and radar data, it makes sense to examine these fields as produced in numerically simulated storms.

Also, how important are ice-phase processes in producing a successful simulation? Low density ice (snow) has been hypothesized as being important in the trailing stratiform region. In the past, difficulties in producing realistic features in the convective region have been attributed to the lack of (high density) ice microphysics in their models (e.g., Miller 1978). However, the inclusion of a complex, realistic ice parameterization is an expensive enhancement to numerical cloud models and needs to be justified.

Two 2D studies which have included ice processes are Yoshizaki (1986) and Lord et al. (1984). Both employed modified versions of the Lin et al. [1983 (LFO)] ice phase parameterization. The former was concerned with simulating a GATE case. He found that by including ice, a trailing region of light precipitation can be obtained. Also, the model storm's propagation speed was found to increase when ice was included; this was attributed to the greater cooling in the subcloud cold pool due to the melting of ice particles. The latter study used an axisymmetric model to simulate a tropical cyclone. They also found that mesoscale features in general were more realistic when ice phase processes were considered.

In this paper, we will focus on the structure of numerically simulated squall lines during the upshear tilting or multicell phase. Simulations made with and without ice processes will be described.

2. Model

The model used in this study is similar to the two-dimensional, anelastic model of Soong and Ogura (1980) which was described in detail in that report. A major difference between their model and ours is that we take the base environemental state to be constant with time, neglecting large-scale motions, surface fluxes and radiation processes. The Coriolis force is also neglected, rendering the model strictly two-dimensional. In addition, open rather than periodic lateral boundary

conditions are used. The boundary conditions we adopted are as described in Klemp and Wilhelmson [1978 (KW)] except for the preseure equation, which requires no boundary condition in KW's fully compressible framework but in the anelastic model is an elliptic equation which is solved diagnostically. The boundary conditions used for the pressure equation are those specified by Ogura and Phillips (1962). Upper and lower boundary conditions are free-slip for all variables except for vertical velocity, which is set to zero.

In all simulations, a stretched vertical coordinate is used in order to maximize resolution in the lowest levels of the model. The resolution of the lowest layer is 200 m; each successive layer is 20 m deeper and the model top is at 21.7 km for the control ice-free run. The control run also used 255 grid points in the horizontal, the central 115 of which comprised the fine grid area with 1 km resolution. Outside of this region, and the grid was stretched; the ratio between adjacent grid spacings was 1.075:1. This results in a domain which is about 4500 km wide. Sensitivity tests were made using fine grid regions of various widths but in all cases the stretched portions of the grid were unaltered.

In practice, Klemp–Wihelmson lateral boundary conditions are controlled by two factors: a gravity wave speed c^*, assumed to be constant, and the gradient of the horizontal velocity approaching the boundary. The boundary condition is applied only if the flow is such that a gravity wave, travelling at speed c^* relative to the ground, could approach the boundary and try to leave the domain. KW found that the behavior of the simulation is sensitive to the choice of c^*; altering it could change a relative inflow to an outflow condition, and vice-versa, with a necessary impact on mass and moisture fluxes. With our horizontal grid stretching the choice of c^* is purely academic; the grid size at the boundaries is large enough to guarantee that horizontal gradients in the airflow are extremely small there.

This means that the domain-relative horizontal flow at the lateral boundaries will resist change and so remain very nearly as it was in the initial state. This has two implications. First, for the eastern boundary, ahead of the storm,the vertical profile of the domain-relative influxes of mass and moisture remain essentially constant over the course of the simulation, which means that the model storm is encountering known and fixed inflow conditions. Second, the stretched grid portions of the domain, both ahead of and behind the model strom, act to relax the storm-perturbed airflow back to the initial state. The net vertical mass flux, integrated over the entire domain, is very nearly zero for each model time step. Since the storm itself produces a net upward mass flux in its immediate vicinity, the stretched grid regions are necessarily marked by descending motion. However, this descent is spread out over a very wide area, roughly 2200 km on each side of the fine grid zone, so that it is of extremely small magnitude. In a sense, then, the stretched grid is acting as an extensive, gentle sponge layer.

Model microphysics are based on the parameterization advanced by LFO with minor exceptions to be noted as appropriate. This parameterization recognizes five forms of condensed water: cloud water, ice crystals, rain, snow and hail. The former two are monodispersed with respect to particle size whereas the others are assumed to be represented by Marshall–Palmer [1948 (MP)] exponential distributions. The snow field consists of low density particles with small terminal velocities while hail is high density, swiftly falling ice. Typical midtropospheric mass weighted fallspeeds for snow, rain and hail are on the order of 2.5, 7 and 12 m s^{-1}, respectively; the ranges for the latter two are wide.

Marshall–Palmer distributions are completely specified by any two of these three parameters: the intercept N_0 (m^{-4}), the distribution slope λ (m^{-1}) and the total concentration of particles N_T (m^{-3}). In the LFO parameterization, N_0 is taken to be a constant for each variable; this yields unique values of λ and N_T for each value of mixing ratio (or mass). In the Cotton parameterization, constant slopes have been assumed (for hail in Cotton et al. 1982 and for snow in Cotton et al. 1986). The choice of the intercept for hail is a particular problem. Knight et al. (1982) reviewed hail intercept estimates determined from samples collected (on the ground) in Colorado and found that for distributions containing particles larger than 1 mm, the intercepts were found to vary over five orders of magnitude. There is also reason to believe that this parameter should not be constant with height. Schmid and Waldvogel (1986) estimated a theoretical hail profile and found that when the effects of melting on the hail distribution is considered, the hail intercept at the melting level can be an order of magnitude larger there than at the surface. This is further complicated by the fact that terminal velocities and microphysical transfer rates are very dependent on the value of this parameter.

Simulations using the value of the hail intercept assumed by LFO (40 000 m^{-4}) have been performed and storms which produced significant hail accumulations, often accounting for 10%–20% of the total surface precipitation, have resulted. Since there were few reports of hail reaching the surface during the OL storm, this is clearly an undesirable result. To counter this, the hail intercept was increased by an order of magnitude. Enhanced melting induced by the resulting decrease in mean particle size all but completely prevented hailstones from surviving to strike the ground in the ice model run to be described later in this report.

These assumed particle distributions can be used to calculate radar relfectivity fields since efficiency in reflection of radar waves is proportional to the sixth power of particle diameter. Such calculations can provide a useful method of verifying model simulations in a far better manner than simply comparing cloud

extent or precipitation amounts. Radar data are far more common than small-scale rainfall records and in-cloud measurements of liquid water content. This tool is particularly useful for simulations which include ice processes due to the number of variables added to the total water field.

Reflectivity estimates generated by the model are calculated using the method of Dye et al. (1974). The effective reflectivity Z_e (mm^6 m^{-3}), after integration over the assumed size distribution, is calculated using

$$Z_e = 720\alpha k N_0 \lambda^{-7} (\rho/\rho_w)^2 \quad (1)$$

where α is the nondimensional ratio of backscattering coefficients for the reflecting substance and liquid water (unity for rain and 0.213 for snow and hail), ρ the density of the substance (kg m^{-3}), ρ_w the density of water and k is the conversion factor (10^{18}) from m^3 to the units of Z_e. Reflectivity in decibels (dBZ) is then given by 10 $\log_{10}(Z_e)$. It can be seen that ice particles reflect radar waves more poorly than liquid water drops due to the smaller backscattering coefficient for ice and, particularly for snow crystals, the smaller densities of ice particles.

The leapfrog scheme with a time step of 5 s was used for all model prognostic equations. Negative water substances created by the scheme were zeroed and the remaining positive values were adjusted each time step so that the total mass of each substance in the domain was conserved in the advection process. Time smoothing was employed in the usual manner to prevent solution separation and the model was monitored for temporal instabilities.

3. Initial conditions

The initial temperature and moisture conditions for these simulations were based on the HNT 1430 CST sounding presented by OL (see Fig. 2). This sounding represented environmental conditions 6.5 h before the squall line passed the station. At low levels, the temperature lapse rate was virtually dry adiabatic and the melting level resided at 3.1 km; these characteristics are typical of many severe springtime storms in this region (Bluestein and Jain 1985). The moisture profile above 750 mb was smoothed before inclusion and no attempt was made to retain the dry intrusions at 700 and 500 mb; at low levels, the profile was modified in order to obtain a mixed layer. The kinks in the temperature profile were also smoothed.

The base state wind profile (Fig. 3) was derived, with modifications, from the composite environment ahead of the storm in OL's Fig. 13. Constant, moderate shear (5×10^{-3} s^{-1}) was used below 2 km; in reality, the hodograph was strongly curved with substantial along-line wind components. This was overlain by layers of smaller shear between 2 and 3.5 km (3.3×10^{-3} s^{-1}) and 3.5 and 7 km (1.4×10^{-3} s^{-1}). Above 7 km the wind shear was taken to zero. This modified wind

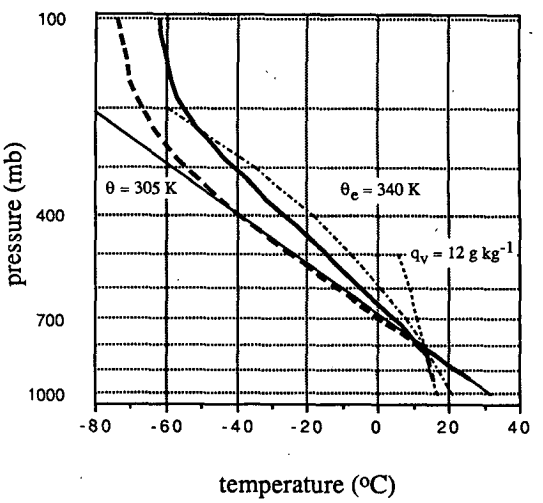

FIG. 2. Initial sounding used in the model simulations. Dark solid line is air temperature and dark broken line is dew point temperature. For reference, the 305 K dry adiabat, 340 K moist adiabat and 12 g kg^{-1} mixing ratio lines have been included.

profile is similar in form to those used by TMM, KRW and others, especially at low levels.

Convection was initiated with a thermal similar to that used by KW. The thermal was 10 km wide and 2 km deep and was centered at 1 km AGL. The maximum potential temperature perturbation was 2 K in the center and sufficient moisture was added to the thermal region so that the relative humidity in the thermal was the same as in the environment.

4. Results—simulations without ice

In this section, the time-dependent behavior and time-averaged structure of a control simulation made without implementing the ice microphysics package are described. Following this discussion, the results of sensitivity tests performed to gauge the impact of model design assumptions and characteristics will be reported.

a. Time-dependent behavior

After initiation, the developing cloud underwent a period in which it attempted to organize. The updraft alternated between vertical and downshear orientations as in the KRW periodically redeveloping phase; during this period the storm was composed of but one cell at and by 60 min sufficient rainwater had evaporated that a well defined surface cold pool had formed. As more rainwater was evaporated in the subcloud region, the pool air became colder and propagated more quickly in the downshear direction. The first suggestion of an upshear tilt in the updraft came around 100 min.
of an upshear tilt in the updraft came around 100 min.

By 225 min the storm had become completely organized and began to resemble the structure of mature storms observed in field studies. Upshear tilt was firmly

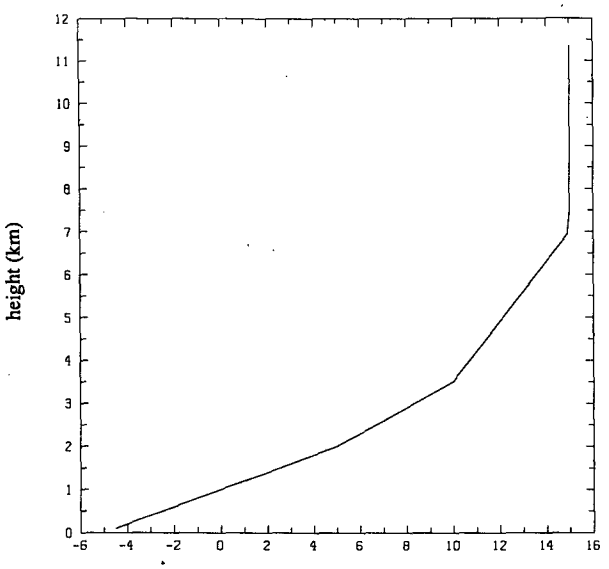

FIG. 3. Base state ground-relative wind profile used in these simulations. Vertical axis is height (in kilometers above ground level). Horizontal axis is the line-normal wind speed (in m s^{-1}).

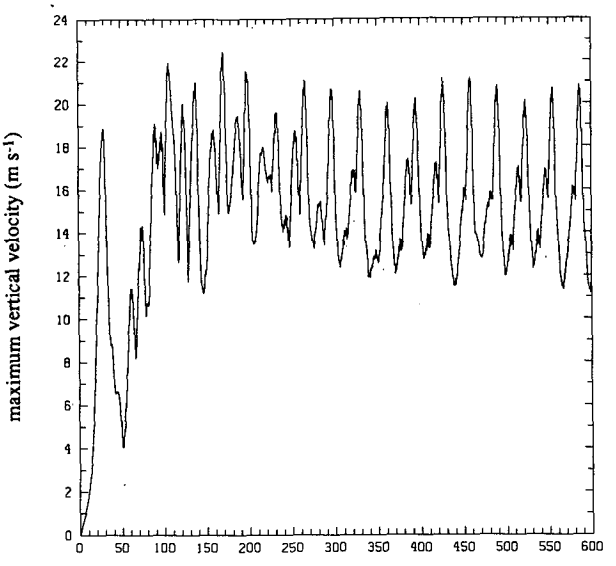

FIG. 4. Time history of the domain maximum vertical velocity (m s^{-1}) for the ice-free run.

established by this time. Surface air cooled by as much as 11.5 K was found in the outflow; this is resonable according to the information of OL. The gust front or outflow boundary (i.e., the sharply defined leading edge of the cold pool) had attained a propagation speed of 14 m s^{-1} relative to the ground and varied from this speed virtually not at all for the remainder of the simulation. This value compares well with the observations.

Figures 4 and 5 present the variation of domain maximum vertical velocity and subcloud minimum buoyancy with time for this simulation. It can be seen that the firm establishment of the upshear tilt marked the beginning of a long and relatively stable period in the life of the system. It was long in the sense that the storm showed no sign of decaying, even though the model was integrated out to 10 h. It was stable in the sense that the maximum vertical velocities oscillated in time in an essentially regular manner around an average value of about 17 m s^{-1}.

During this portion of the simulation, which we will refer to as its "mature phase," the storm was multicellular, characterized by the periodic development of cells at the leading edge of the storm. As in the observations, these cells grew out of the forced lifting over the gust front. The cells' maximum updrafts intensified and rose vertically as they propagated rearward in the airflow which consisted of environmental air drawn from low levels and accelerated over the outflow cold pool.

The periodic behavior seen in Fig. 4 is also observable in Fig. 6 which portrays the time history of rainfall intensity at the surface for the latter 5 h of the simulation. The horizontal axis represents a 90 km wide section of the fine grid region of the domain. Rainfall intensity was computed as 2 min averages of actual precipitation and is expressed in mm h^{-1}. It is important to note that these averages were computed in a domain-relative sense. In this figure, the coordinate system translation speed is eastward at 14 m s^{-1}, the same speed as the line was found to move.

The time interval between major precipitation bursts in this figure is very nearly 33 min. It can be seen that

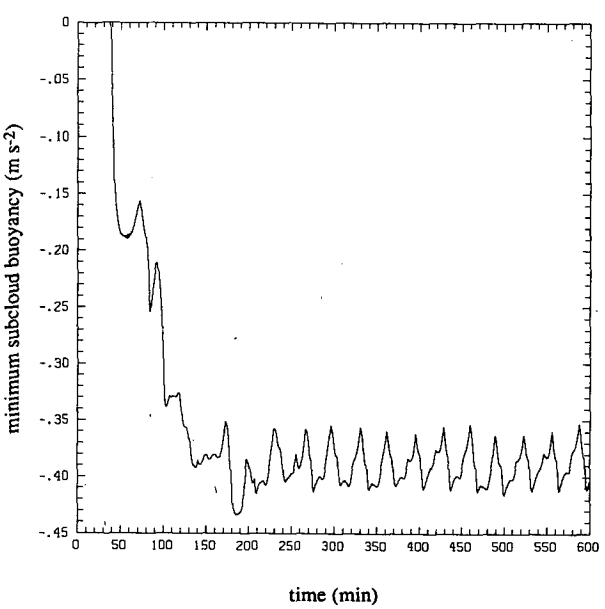

FIG. 5. Time history of the minimum buoyancy in the model storm's subcloud outflow (m s^{-2}) for the ice-free run.

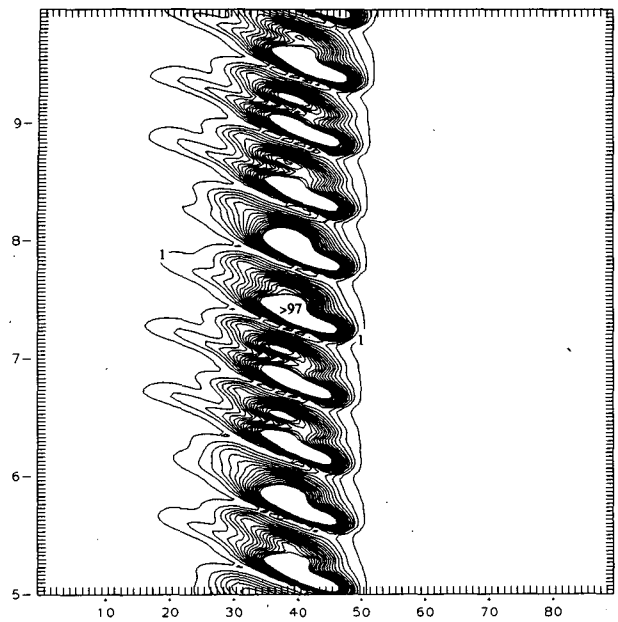

FIG. 6. Surface rainfall intensities (mm h^{-1}), computed as averages of actual precipitation over 2 min intervals, for the ice-free run between 5 and 10 h. Intensities are domain-relative (i.e. system-relative) rather than ground-relative; domain speed is 14 m s^{-1}. The horizontal axis is a 90 km section of the model fine grid region; ticks are spaced 1 km apart. The vertical axis represents time (increasing upward); ticks are 2 min apart. Contour interval is 6 mm h^{-1} between 1 and 97 mm h^{-1}; for emphasis, contours above this value were deleted.

each burst began near the leading edge of the storm and moved rearward with time. Superimposed on this oscillation is another with a period of just over 2 h. This longer oscillation is most apparent in the appearance of the small local precipitation maxima which occurred between (and was sometimes obscured by) the major bursts.

Figures 7 and 8 portray a time sequence of model estimated radard reflectivity and system-relative airflow for the 32 min period between 390 and 422 min, which approximately encompassed one repeat cycle. In this ice-free case, radar reflectivity is a funciton of rainwater content alone. In Fig. 7a, four cells can be seen. Near the front of the storm, above x = 45 km on Fig. 7a, there is a new cell, or first echo, which has formed above and behind the gust front boundary (located above x = 51) at a height of 3.1 km. This echo appeared several minutes earlier and had been intensyfying rapidly. Further rearward are a mature cell above x = 36 (maximum reflectivity > 55 dBZ), a decaying cell above x = 23 (45 dBZ) and a still older cell above x = 0 with a small amount of rain water trapped in its residual updraft.

Subsequent panels in this figure, each separated by 8 min, show that the new echo first intensitified and then decayed as it moved rearward relative to the gust front. During the cell's intensifying phase, the cell-gust front separation speed was approximately 10 m s^{-1}, close to the 9 m s^{-1} value reported by SH1. By 422 min (Fig. 7e), one minute shy of the observed repeat cycle, another new echo formed at the leading edge. The location of this echo relative to the gust front is the same as for the new echo of Fig. 7a; this is similar to the mature phase behavior documented by Sanders and Emanuel (1977) in another Oklahoma case. Although this multicell storm is surviving through the periodic production of new cells, this behavior allows us to unambiguously specify the model system's propagation speed as that of the gust front. The repetitiveness achieved by the model storm during this phase is again underscored by a comparison of Figs. 7a and 7e.

The vertical shape of these cells has been determined by the storm's airflow (Fig. 8). In between the mature and growing cells in Figs. 7a and 7e, two echo-free regions existed, above x = 41 and x = 43. The former, directly in front of the mature cell, has the appearance of a typical multicell storm vault; it appeared only briefly and the high reflectivity portion of the mature cell wrapped around its top. It can be seen in Fig. 9a that the air in both of these vaults came from the low θ_e (equivalent potential temperature) layer in the mid-level inflow environment, the stippled area on the figure. This vault obtained its shape as the explosively growing new cell pinched off a pocket of this air. Between the times of Figs. 9a and 9b, some of this low θ_e air was mixed into the mature cell, which had entered into a state of rapid decay. This decay was induced as a consequence of the new cell's modification of the storm airflow; the mature cell was ingesting this low θ_e air and was cut off from the moisture-laden air from near the surface.

The sudden weakening of the mature cell's updraft allowed a large amount of rainwater that had been trapped in the updraft to fall out, contributing to the establishment and intensification of a low-level downdraft beneath the cell. This aspect of the model storm behavior is essentially the same as has been described in DMS as well as in Nicholls (1987). This cell's downdraft reached its maximum intensity of about 6 m s^{-1} at 398 min, the time of Fig. 8b, and continued to propagate rearward underneath with the dying updraft which was its source. The magnitude of the downdraft weakened after this time as the supply of rainwater feeding it diminished.

The low θ_e air pocket from the echo vault was eventually incorporated into this downdraft and was drawn into the cold air outflow beneath the cloud, whereupon it was carried towards the front of the storm in the subcloud airflow. This is demonstrated on the figures by the progress of an air parcel (depicted by the black dot) which had arrived at the vault from the environment ahead of the storm at the time of Fig. 9a. It is obvious that, given the general airflow shown in Fig. 8, much of the low θ_e air behind the gust front could have come directly from the rear. Our calculation shows, however, that of the total amount of low θ_e air

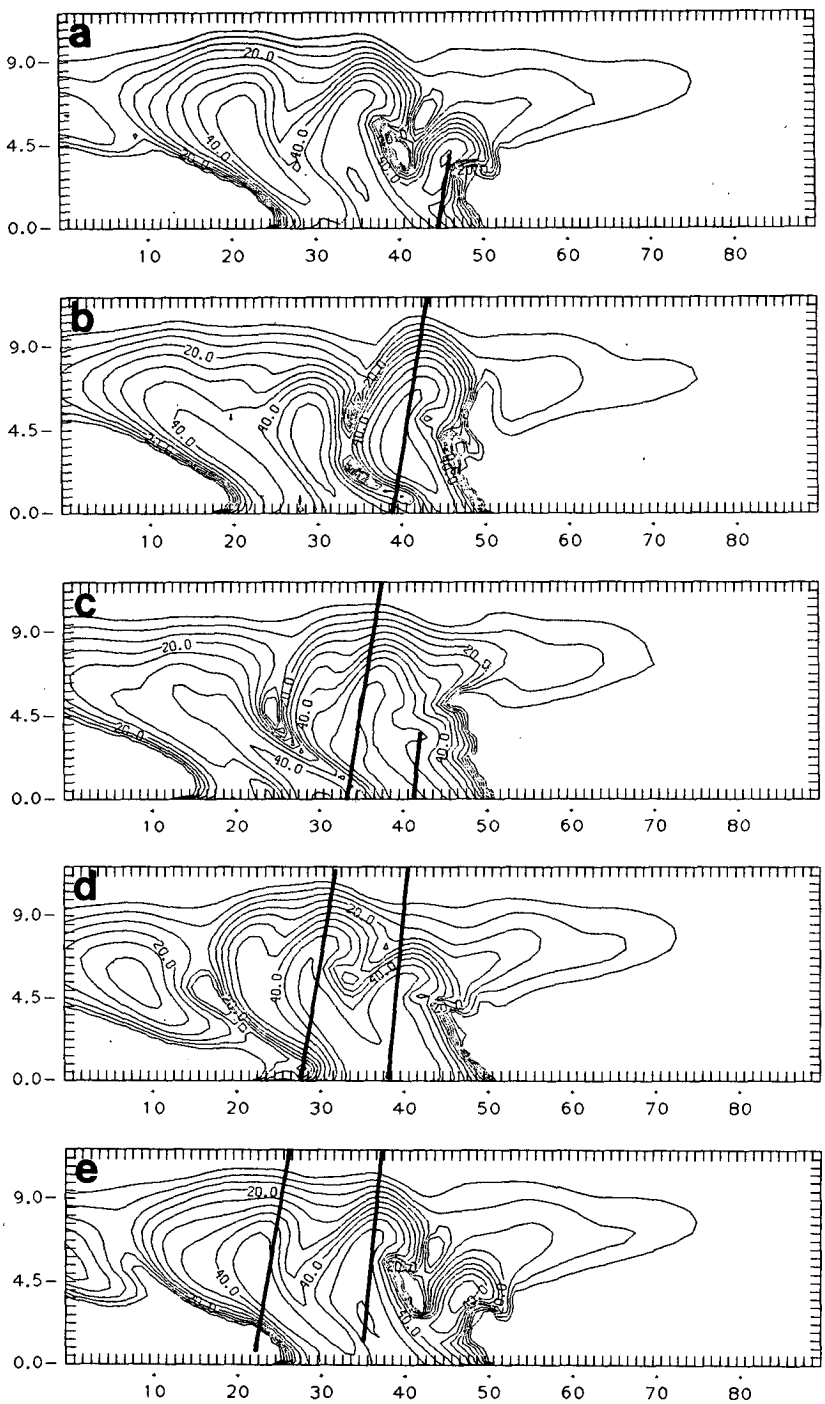

FIG. 7. Model estimated radar reflectivity (dBZ) presented at 8 min intervals between 390 and 422 min model time. The same 90 km section of the domain as in Fig. 6 is displayed. The tick marks on the vertical axis are 450 m apart; only the tropospheric portion of the domain is shown. The contour interval is 5 dBZ.

incorporated into the cold pool during the repeat cycle, approximately 29% came from the midlevel environment ahead of the storm, despite the two-dimensionality of the model storm structure.

In Fig. 10a, which shows the vertical velocity field at 390 min, it can be seen that the mature and newly established cells were separated by a deep zone of downward motion, extending from the tropopause (the

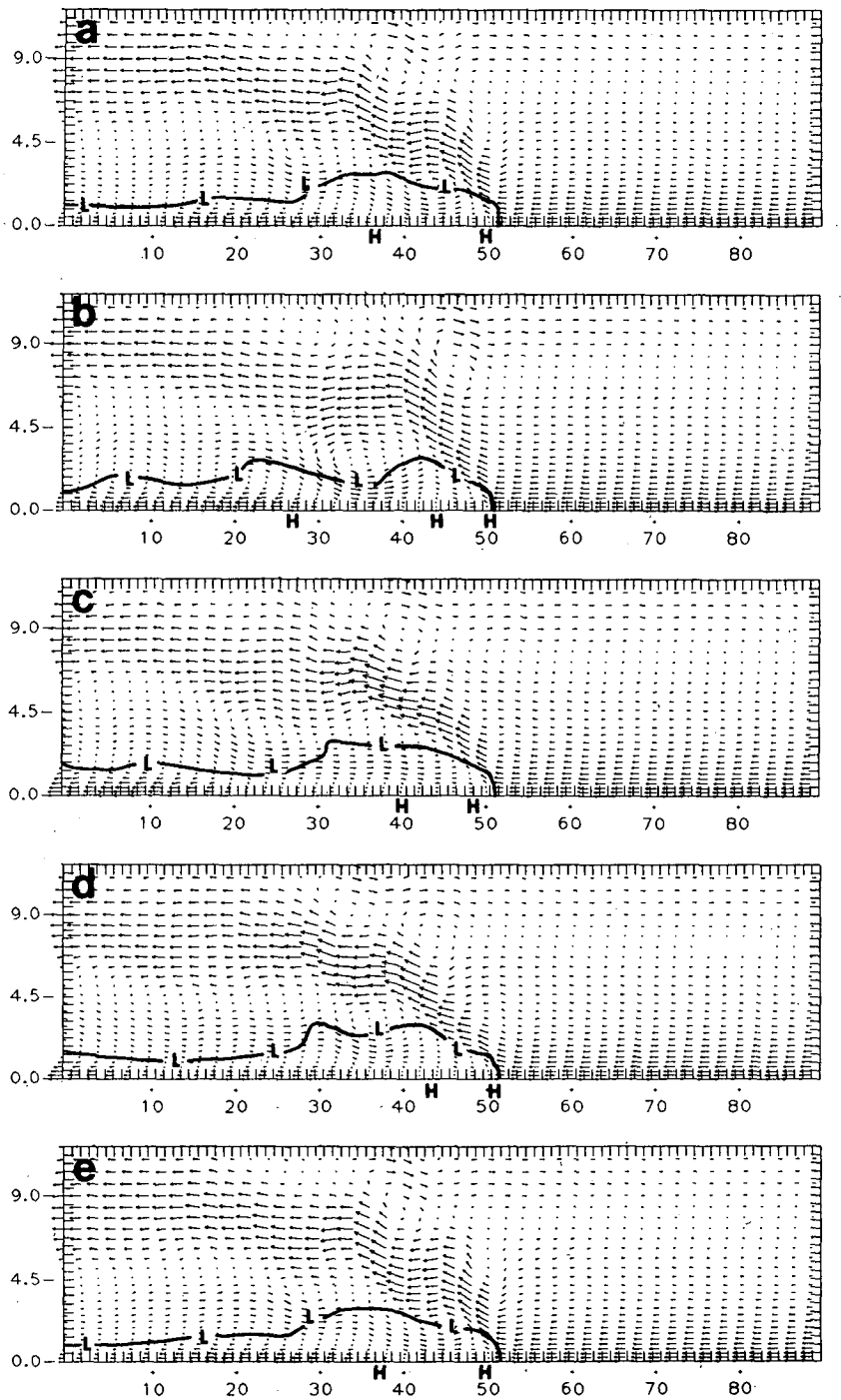

FIG. 8. System-relative airflow presented for the same times as in Fig. 7. For clarity, only alternate grid points in the horizontal were plotted. Vectors have been scaled such that one the length of a grid interval represents 14 m s^{-1}. The letters "L" and "H" mark locations of local midlevel minima and surface maxima of pressure, respectively. On each panel, the heavy black line shows the instantaneous outline of the storm's cold air pool (where the potential temperature deviation from the initial state was zero); chilled air resided beneath this line.

top of the figure) to the surface. This downdraft was composed of three parts which were essentially separate at this time. At 9 km, the downward motion was due to the deceleration of mass ejected from the top of the mature cell; this convergence zone can be noted in Fig. 10b, which presents the system-relative horizontal ve-

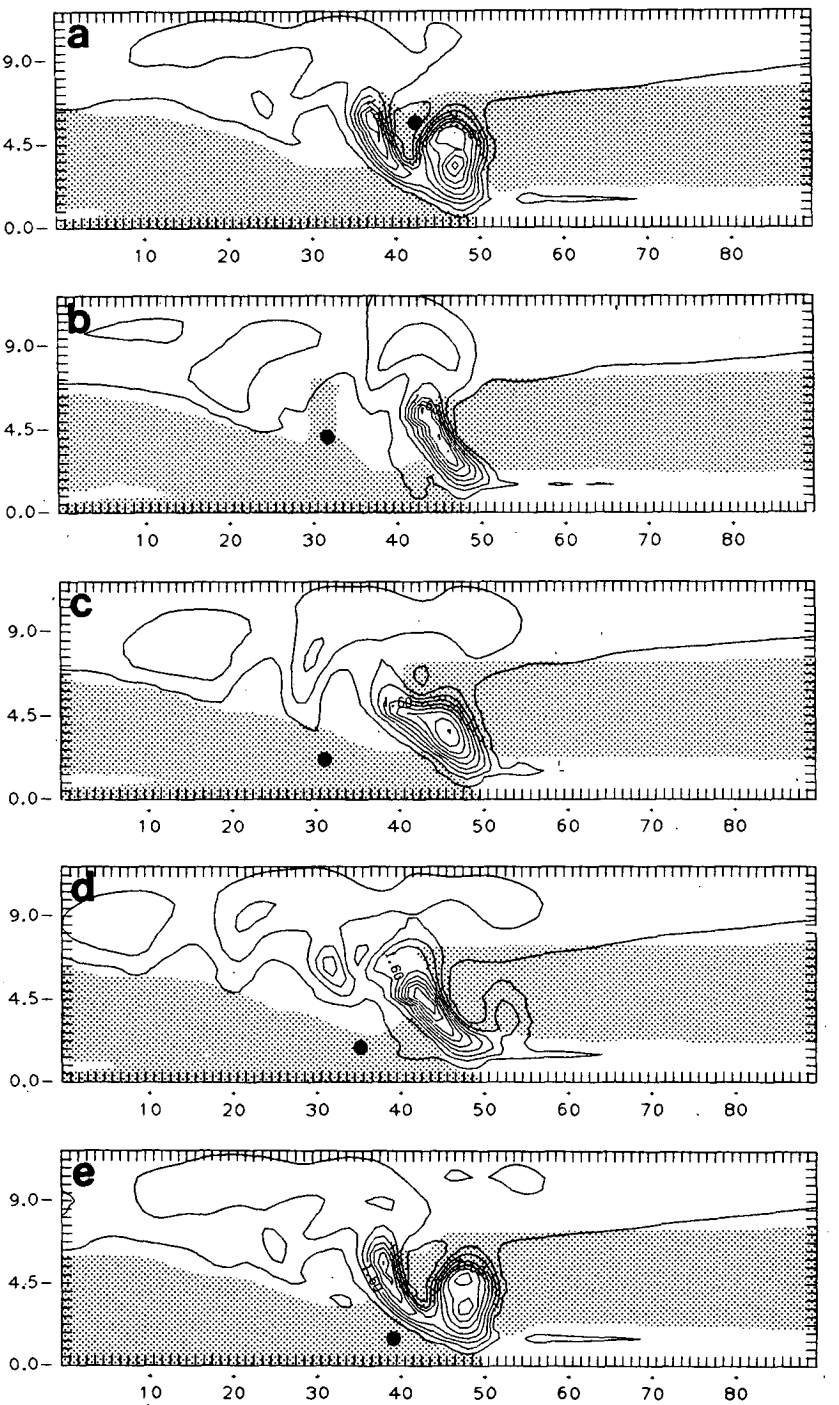

FIG. 9. As in Fig. 7 but for cloud water mixing ratio; contour interval 0.5 g kg^{-1} starting from 0.1 g kg^{-1}. Stippled region encloses air with equivalent potential temperatures (θ_e) less than 327 K. Black dot on each panel represents the location of an air parcel which had entered the system from the low θ_e environment ahead of the storm at the time of the first panel.

locity field at this time. Such high-level downdrafts have been observed by, for example, Heymsfield and Schotz (1985) and SH2, although the inability of the ejected air to move out of the 2D plane undoubtedly played a role as well.

This downdraft differed from the other two components in that it consisted of high θ_e air. The midlevel section was composed of the slightly negatively buoyant low θ_e air of the vault previously described, and the low-level draft was that which was developing beneath

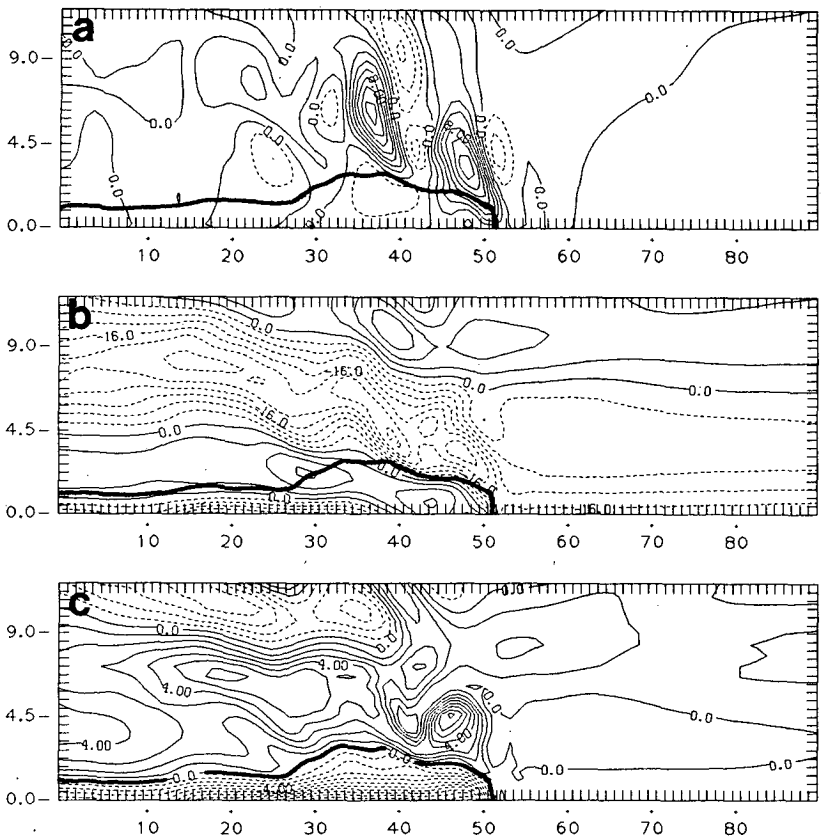

FIG. 10. Instantaneous model fields at 390 min. (a) Vertical velocity (contour interval 2 m s^{-1}). (b) System-relative horizontal velocity (4 m s^{-1}). (c) Potential temperature deviation from the initial state (1 K). The subdomain pictured is the same as in Fig. 7. Heavy black line denotes the outline of the subcloud cold pool, as in Fig. 8. Dashed lines represent negative values.

the mature cell. Figure 10c, which presents the potential temperature field (expressed as a deviation from the base state) at this time, emphasizes both this vault air and the discreteness of the rapidly developing new cell. The two low θ_e zones of Fig. 9a were separated by a ribbon of high θ_e air that was snapped in the next few minutes, isolating the old cell updraft and allowing these two zones to merge. Note that by the end of the repeat cycle (Fig. 9e), the air parcel from the vault downdraft had been carried into what was by then the rapidly dissipating mature cell's low-level downdraft.

Rearward of the developing downdraft in Fig. 10a are the remnants of an older updraft–downdraft pair. The location of this pair, above $x = 25$, corresponds with the older, weaker cell in Fig. 7a. While the downdraft component of the pair was embedded in low θ_e air, like the downdraft of the decaying major cell, it was not being supplied with rainwater for evaporation at a rate sufficient to compensate for adiabatic warming due to the subsiding motion, with the result that the air within it was positively buoyant. This warming helped to maintain the zone of low-to-midlevel positive temperature perturbations, which can be seen at the rear of Fig. 10c; it will be shown later that the air in this draft was highly unsaturated at this point in its existence.

The first echoes of Figs. 7a and 7e developed into the cells which produced major precipitation bursts as seen in Fig. 6. The smaller bursts which occurred in between were produced by "secondary cells" that did not attain the same degree of development in terms of reflectivity, updraft and precipitation production as did the other (major) cells. The development of such a secondary cell can be seen in Figs. 7c and 8c (406 min) above $x = 42$. It did not appear as an isolated first echo and, apart from the fact that it did develop its own, distinct radar signature at subsequent times in the figure, it is not entirely clear in Figs. 8 and 9 that it was a truly dynamically separate entity from the previous major cell. In any case, the failure of the secondary cell to achieve full development may be due to its relatively late appearance in the 33 min cycle; the cell was cut off from the low-level inflow by the next major cell before it had a chance to fully intensify. The major cell

which appeared in the radar field at 422 min (Fig. 7e) can be seen as early as 414 min in the cloud water field (Fig. 9d).

The 33 min repeat cycle of Fig. 6, then, consisted of two cells—major and secondary. The major cells produced intense rainfall, exceeding 100 mm h^{-1} for an average of 15 min, with a typical maximum value of 190 mm h^{-1}. The major/minor cell pair appeared in each repetition, although in several of the bursts the rain produced by the secondary cells was not well differentiated from that of its associated major cell, giving those intense bursts the elongated appearance of a footprint in Fig. 6. The longer oscillation in this figure is manifested by small differences in the relative time within each repeat cycle that the secondary cell appeared and the degree to which it was able to develop before being cut off from the low-level inflow.

b. *Time-averaged structure*

A common objective in field studies of convective systems is the determination of mass and moisture fluxes through the storm (e.g., Newton 1966; Heymsfield and Schotz 1985). In addition, we desire information about the structure of the model storm at scales larger than that of the individual cells. Both objectives can be accomplished by averaging the model fields, in a system-relative sense, over a period of time longer than that of the cell regeneration period.

The panels of Fig. 11 depict distributions resulting from averaging over a time period containing four complete 33 min repeat cycles (encompassing four major and four secondary cells). The fields were constructed by averaging data which was archived at 2 min intervals. The fields of potential temperature (Fig. 11a) and water vapor mixing ratio (Fig. 11b) represent deviations from initial conditions and the horizontal velocity field (Fig. 11c) is system-relative. The thick solid line on each figure is the outline of the time-averaged subcloud cold pool.

As did the time-dependent fields, these distributions show that the leading edge of the model storm slanted rearward with height to an appreciable degree. This edge is best discernible in Fig. 11a as the zone where large horizontal temperature gradients between the relatively undisturbed environment and the cloud modified air existed. Cloud-layer air in the active convection region, where the cells tracked in previous figures resided, was moist as well as warm (Fig. 11b) and the horizontal relative flow through it was front-to-rear (Fig. 11c). In the cold subcloud zone, airflow was primarily rear-to-front near the leading edge where the cold pool was deep and front-to-rear farther behind where it was shallow. The forward moving air met incoming warm air from the environment at the gust front, and the collision forced upward turning of the flow on both sides of this boundary.

The time-averaged updraft maximum was found to be located at low levels, just above the cold air pool (Fig. 11d). This was in part due to the averaging process which smoothed out the higher level updrafts associated with the transient, mature cells. Inflowing air was lifted over the cold outflow pool and accelerated rearward in the process; the fastest winds in absolute magnitude in the storm in Fig. 11c were located in the rearward flow above the cold pool 11 km behind the surface gust front position. The maximum rearward wind speed ($\sim$27 m s^{-1}) exceeded that of the fastest system-relative inflow winds in the environment ahead of the storm (18.5 m s^{-1}).

Figure 11e presents the time-averaged perturbation pressure field, $p^*(x, z)$, deduced from the averaged velocity, temperature and moisture fields. The boundary between the warm cloud air and the cold subcloud region was the location of a pressure minimum. This minimum, which had a magnitude of approximately -3 mb, was displaced behind the leading edge and very similar pressure fields have been found in field studies of tropical lines such as LeMone (1983) and LeMone et al. (1984), although the intensity of the minimum in our case was substantially larger than what they found. As in those studies, this pressure field was found to be very nearly in hydrostatic balance throughout the bulk of the storm; the vertical gradient field (not shown) closely resembled that of the time-averaged perturbation potential temperature (Fig. 11a) which dominates the perturbation buoyancy term. Departures from *time-averaged* local hydrostatic balance, expressed as a vertical acceleration in Fig. 12a, were found to be mainly centered in a narrow zone at and just ahead of the outflow boundary where the collision of warm and cold air dynamically forced upward motion. We should again note that the pressure field in Fig. 11e was diagnosed from the time-averaged fields. In the time-dependent flow, each cell had its own distinct pressure minimum which moved rearward with it; this could be seen in Fig. 8. The propagation of pressure minima along the top of the cold outflow resembles the situation found in the numerical simulations of density currents of Droegemeier and Wilhelmson (1987) who found these minima to be cyclostrophically balanced.

The acceleration of the horizontal airflow associated with the horizontal pressure gradient is shown in Fig. 12b. It can be seen that the rearward acceleration of storm inflow air over the outflow was associated with the pressure gradient directed into the low pressure area behind the leading edge. On the back side of the low, the pressure force contributed to a deceleration of the rearward flow, producing a convergence zone directly above the pressure minimum corresponding to the horizontal wind maximum noted earlier. At the rear of the storm, the horizontal pressure gradients were small.

The pressure field can be further analyzed by subdividing it into its dynamical (p_d^*) and buoyant (p_b^*)

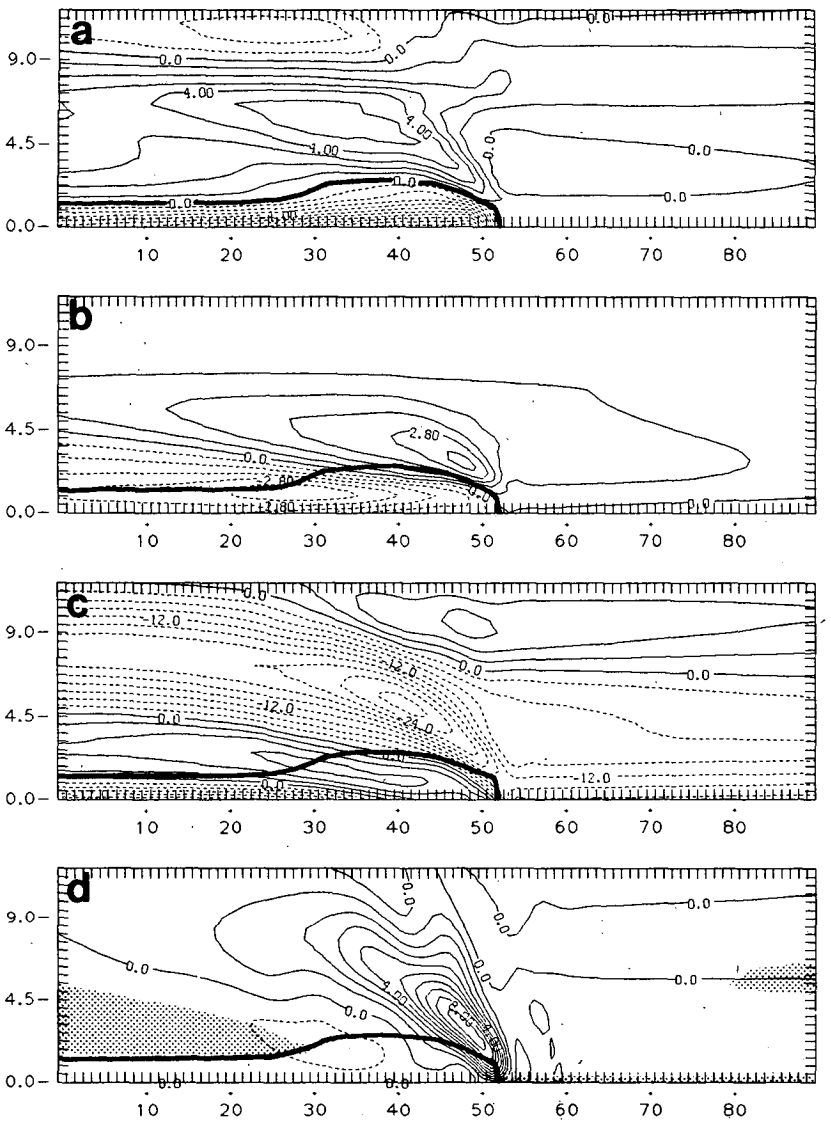

FIG. 11. Time averaged fields for the ice-free case, averaged in a system-relative sense over an integral number of cell developments. (a) Potential temperature deviation from initial state (contour interval 1 K). (b) Water vapor mixing ratio deviation from initial state (0.7 g kg^{-1}). (c) System-relative horizontal velocity (3 m s^{-1}). (d) Vertical velocity (1 m s^{-1}); stippling shows where air with relative humidities (with respect to liquid water) $\leq$ 60% resided. (e) Perturbation pressure (0.4 mb). (f) Airflow pattern derived from averaged horizontal and vertical wind fields. (g) Radar reflectivity (5 dBZ). (h) Equivalent potential temperature (3 K). The outline of the subcloud cold pool from the time-averaged field in panel (a) has been superimposed on each panel. Dashed lines denote negative values.

components, as had been done by Wilhelmson and Ogura (1972). The dynamical component p_d^* reflects pressure associated with the deformation of the wind field and is depicted in Fig. 12c. Here, our p_b^*, shown in Fig. 12d, includes the drag pressure associated with liquid water which was evaluated separately by Wilhelmson and Ogura.

The dynamic component contributed approximately a third of the −3 mb pressure minimum in the active convection region. That the pressure field was mainly hydrostatic with respect to the vertical structure can be seen again in Fig. 12c in that the vertical gradients of p_d^* were much smaller than the vertical gradients of p_b^* (Fig. 12d) except, as noted previously, right at the gust front boundary. The arrangement of high dynamic pressure at the outflow edge at the surface with high buoyancy (mostly hydrostatic) pressure further behind resembles typically observed surface pressure distri-

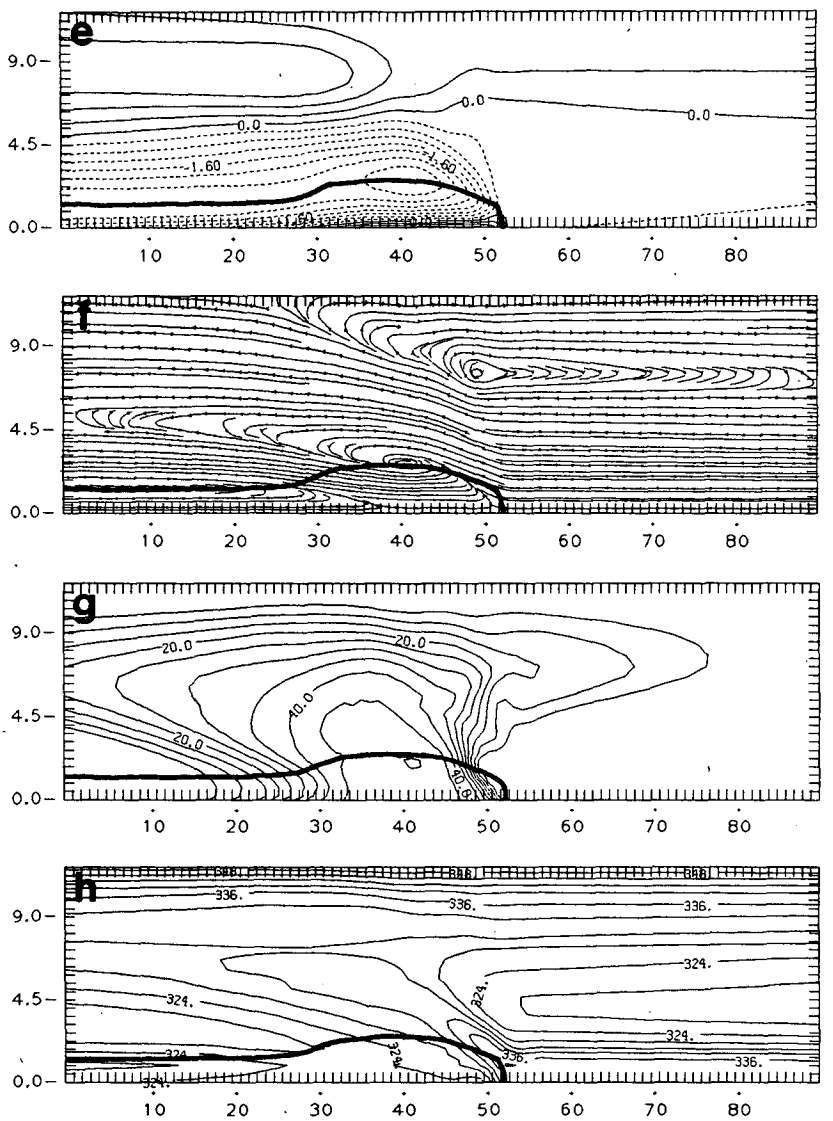

FIG. 11. (*Continued*)

butions during outflow passages (e.g., Wakimoto 1982, Fig. 24). It is clear, however, that the dynamic component contributed a non-negligible portion of the pressure-associated acceleration of horizontal momentum.

The assessment of the contributions of various terms in the horizontal momentum or acceleration budget has been a part of the field studies of LeMone (1983) and SH2 and also numerical studies such as that of Soong and Tao (1984). Our presentation of these terms will differ from the above cited studies in that we will examine accelerations associated with, and deviations from, the time-averaged (rather than space-averaged) storm airflow. The Eulerian horizontal acceleration equation, integrated over the averaging period τ can be written (neglecting viscosity terms and the products of perturbations with mean values) as

$$\underset{\text{A}}{\frac{(u_f'' - u_s'')}{\tau}} = \underset{\text{B}}{-\frac{\partial u_m u_m}{\partial x}} \underset{\text{C}}{-\frac{\partial \rho_b u_m w_m}{\rho_b \partial z}} \underset{\text{D}}{-\frac{\overline{\partial u'' u''}}{\partial x}} \underset{\text{E}}{-\frac{\overline{\partial \rho_b u'' w''}}{\rho_b \partial z}} \underset{\text{F}}{-\frac{\partial p^*}{\rho_b \partial x}} \quad (2)$$

where $u(x, z, t) = u_m(x, z) + u''(x, z, t)$ and $u_m(x, z) = u_b(z) + u^*(x, z)$. The subscripted variables on the right hand side of (2) were those depicted in Fig. 11; deviations represent correlations due to the transient

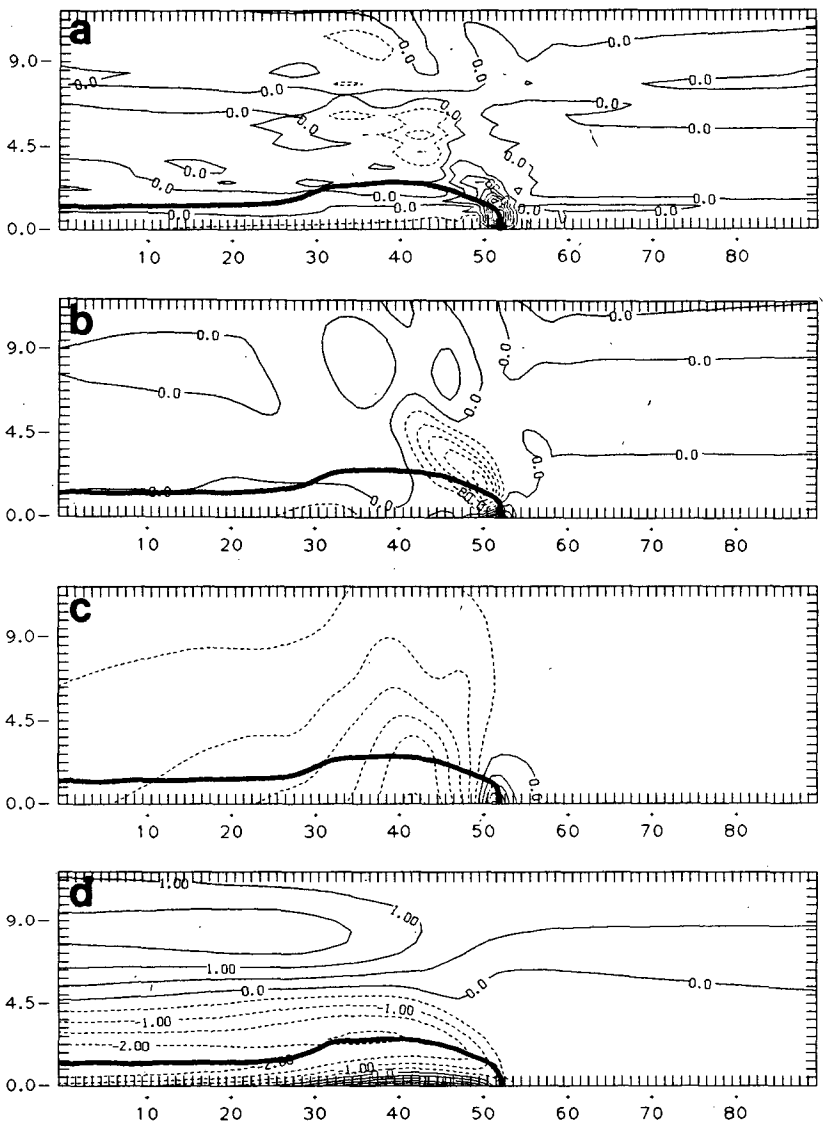

FIG. 12. Additional time-averaged fields for the ice-free case. (a) Nonhydrostatic local vertical perturbation pressure acceleration (contour interval 30 m s^{-1} h^{-1}). (b) Horizontal perturbation pressure acceleration [Term F of horizontal acceleration equation] (40 m s^{-1} h^{-1}). (c) Dynamic pressure component of time-averaged perturbation pressure field (0.2 mb). (d) Buoyancy pressure component of the time-averaged perturbation pressure field (0.5 mb). (e) Term C of horizontal acceleration equation (100 m s^{-1} h^{-1}). (f) Terms B and C combined (50 m s^{-1} h^{-1}). (g) Terms D and E combined (10 m s^{-1} h^{-1}). (h) Horizontal vorticity field deduced from time averaged data (0.003 s^{-1}).

cells. The values of u_s'' and u_f'' were instantaneous values from the start and finish of the averaging period, respectively, and ρ_b is the base state air density, a function of height only.

Term A (not shown) was much smaller (maximum $\sim$ 10 m s^{-1} h^{-1}) than the other terms, reflecting the repetitiveness of the model storm which allowed us to average in time. Term C, the vertical divergence of the vertical flux of the time-averaged wind, is depicted alone in Fig. 12e and combined with Term B in Fig. 12f. These terms were nearly equal and opposite, and the combination compensated for much of the rearward acceleration associated with the pressure force (Term F) presented in Fig. 12b. Differences between these figures reflect the contribution due to transient motions (Terms D and E, combined in Fig. 12g). The terms on the right-hand side of the equation very nearly balance throughout the storm, except right above the

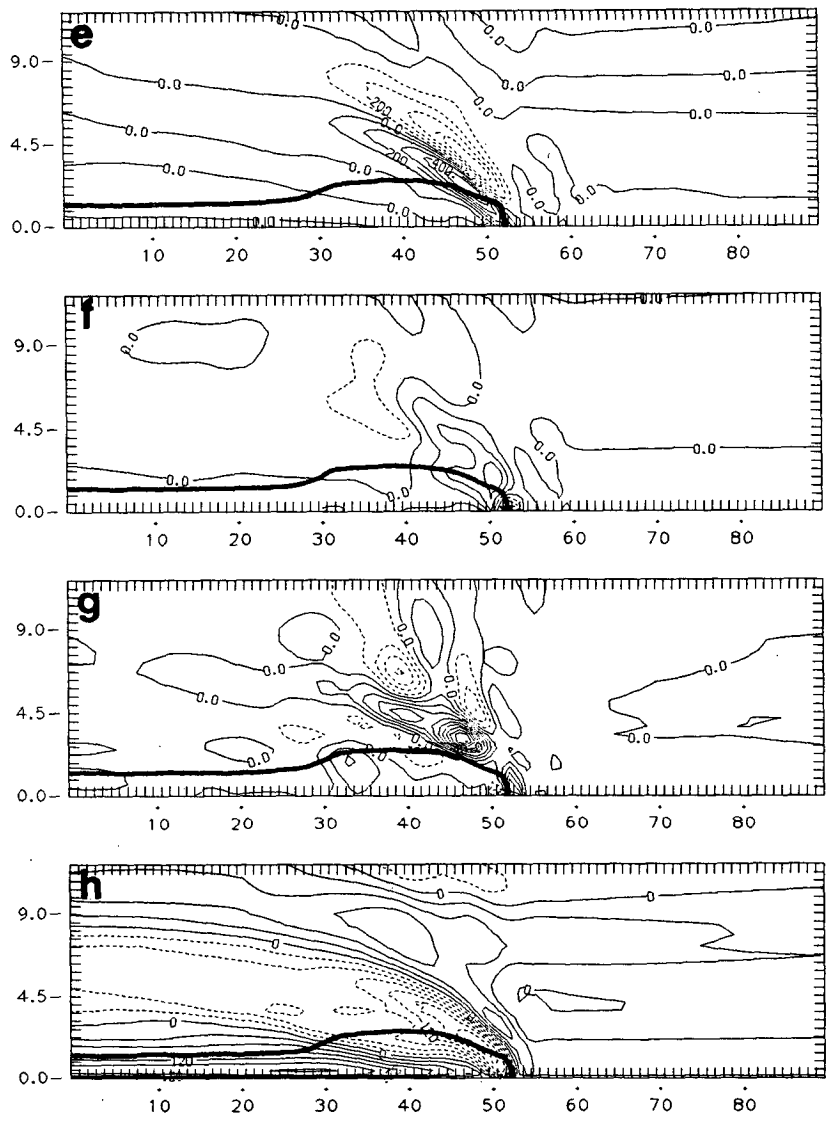

FIG. 12. (*Continued*)

surface at the gust front, indicating that the excluded perturbation and viscosity terms were negligibly small, as would be expected.

Figure 11f shows the system-relative airflow pattern deduced using the time-averaged velocity fields. This pattern is qualitatively similar to the circulation model presented in DMS. The low pressure behind the leading edge is clearly visible as the center of an apparent rotor-type circulation feature. Some of the air ingested by the storm in the upper branch of the rotor descended over a wide region at the rear and combined with a forward-directed current of air entering from the rear to feed the lower branch of the rotor in the cold pool. A portion of the air in this rear inflow current returned to the rear once it entered the cold air pool, forming the overturning downdraft component of the DMS model. The layer of descending motion at the rear (Fig. 11d) was continuously fed by the downdrafts which developed beneath the rearward traveling cells, as noted earlier.

The cold pool itself extended far to the rear, settling to a depth of about 1.4 km. The pool possessed low θ_e values (Fig. 11h), indicating it was composed of air of midlevel origin, and the horizontal buoyancy differences across the outflow boundary generated negative horizontal vorticity (Fig. 12h). As noted earlier, the obvious source region of this low θ_e air was from the rear, advected forward within the aforementioned rear inflow current; this situation was also modeled by, for example, DMS. Recall, however, that it was demon-

strated that a significant fraction of this air did enter the storm from the front and was deposited into the subcloud cold pool by cell downdrafts; this is no longer clear in the figure due to averaging.

At the rear, above the top of the shallow body of the cold pool, the downdrafts from the decaying cells propagated rearward into the subsidence region which was marked by adiabatic warming and drying (for $x < 30$ in Figs. 11a and 11b), as previously examined. (While subsiding motion did occur over a wide region of the rear, we will adopt DMS' term "subsidence region" to refer to this particular area since adiabatic warming obviously dominated evaporational cooling there.) The downdrafts were highly unsaturated in this region; the stippled areas in Fig. 11d show where the air was quite dry (with relative humidities $\leq 60\%$). The combination of the adiabatic and advective effects of downdraft and the rearward spread of evaporatively cooled air from the leading portion of the storm is known to produce the familiar "onion" shaped vertical profile of temperature and moisture observed by OL in this case and by Zipser (1969, 1977) and others in the trailing regions of many other squall lines.

Figures 13a and 13b show the horizontal and vertical mass fluxes as a function of height. The horizontal fluxes were calculated using the initial wind field adjusted to be system-relative (the curve labeled "base state") and the model predicted horizontal wind components at the right ("front") and left ("rear") sides of Fig. 11c. These boundaries were about 40 km ahead of the surface gust front and 15 km behind the surface trailing echo (see Fig. 11g) of the time-averaged model storm, respectively. Negative values represent flow *into* the storm. The vertical fluxes were calculated within this subdomain.

At the front of the storm, storm induced forward airflow above about 7 km produced a leading anvil. The height of the anvil base agrees well with the observations of OL despite the fact that the jet at this level was removed. At the rear, it can be seen that mass was expelled out through a deep layer above 4.5 km and also through a shallower layer bounded from above by the top of the cold air pool. The former, representing the enhancement of front-to-rear airflow compared to the system-relative inflow environment, has been an observed feature of squall line circulation since Newton (1950). We will refer to this feature as the mesoscale front-to-rear jet. The latter is the rearward branch of the overturning downdraft of the DMS model.

Between these two layers resided the current of system-relative rear inflow referred to earlier. Midlevel inflow currents such as this have been noted in observational studies of midlatitude (e.g., Newton; SH3) and tropical (e.g., Zipser 1969; Chong et al. 1987) convective lines and have appeared in numerical simulations as well (e.g., DMS; Nicholls 1987). A comparison of Figs. 11a and 11c shows that this current entered from the back of the storm above the body of the cold pool and thus consisted of warm, dry air in the subsidence region. Farther forward, this current descended as the cold pool itself deepened. The descent of the current into the cold pool, which marks the forward boundary of the subsidence region, was forced by the stronger,

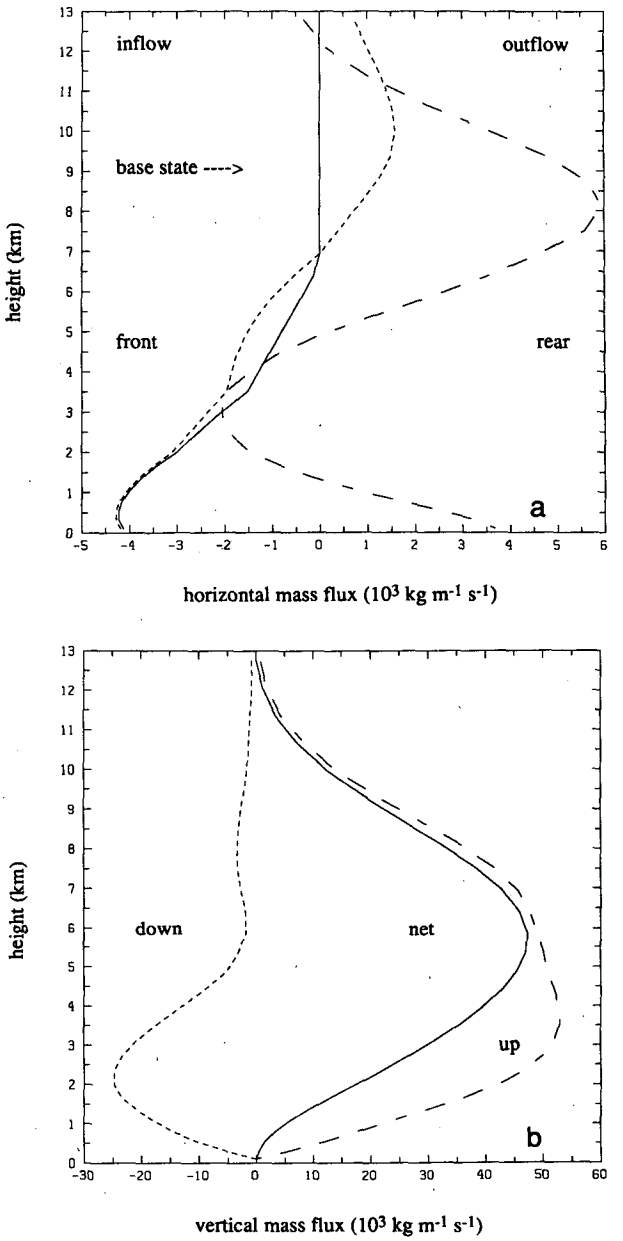

FIG. 13. Time averaged mass fluxes (kg m^{-1} s^{-1}) in the (a) horizontal and (b) vertical for the ice-free run. In (a) the curve labelled "base state" was calculated using the initial wind profile adjusted to be system-relative. The curves labelled "front" and "rear" used model estimated system-relative winds at the right and left boundaries, respectively, of the subdomain pictured in Fig. 11c. Outflow from the subdomain is positive; inflow negative. In (b), the vertical mass flux was computed in the 90 km subdomain.

negatively buoyant downdrafts which developed beneath the convective cells.

This rear inflow current became established slowly over time during the model storm's organizing phase. As the front-to-rear jet developed so did the inflow current; both spread towards the rear with time. The *location* of the current layer in the vertical can be attributed in part to the forward-directed pressure gradient into the low pressure area behind the leading edge. However, it is believed that the *intensity* of this inflow was a consequence of the assumptions of incompressibility and two-dimensionality, and the upper and lower boundary conditions used in the model. The elliptic pressure equation is solved diagnostically each time step to provide the pressure field that maintains the validity of the anelastic continuity equation $\partial \rho_b u/\partial x + \partial \rho_b w/\partial z = 0$. With upper and lower rigid boundaries this requires (by Green's theorem) that the vertically integrated horizontal mass flux through any vertical plane in the domain must be the same and unchanged from the initial state. In this case, low-level environmental horizontal momentum, transported vertically over the outflow and augmented by pressure effects, was carried rearward requiring forward directed airflow to maintain continuity. The location of this compensating rear inflow current was determined by the pressure field.

The most serious of these model constraints is two-dimensionality. The others are not unreasonable if acoustic transports can be assumed to be small, the surface terrain smooth and the vertical column is taken to be sufficiently deep such that the vertical velocity vanishes at the top. However, if the rearward directed airflow had been allowed to turn out of the plane, the compensating inflow might have been substantially reduced or altered in orientation. An inflow current making a more acute angle to the line would have brought forward air which was more moist than that which resided directly to the rear in the warm, dry subsidence region. This should have some impact on the storm as it would influence the composition of the air in the cold pool.

In Fig. 13b it can be seen that the updrafts and downdrafts which have persisted through the averaging process were maximized at low levels. The latter, along with Fig. 11d, indicates that a wide area of descending motion, mesoscale in extent although quite deep when compared to the observations, was present at the rear of the model storm.

Figures 14a and 14b show the moisture fluxes through the boundaries of the subdomain during the averaging period. Water vapor was found to flow into the storm from ahead at a rate of 424 kg m^{-1} s^{-1} and a small, additional amount was provided by the rear inflow current. This total influx is slightly greater than the 382 kg m^{-1} s^{-1} expected from the base state environmental moisture and (system-relative) wind profiles

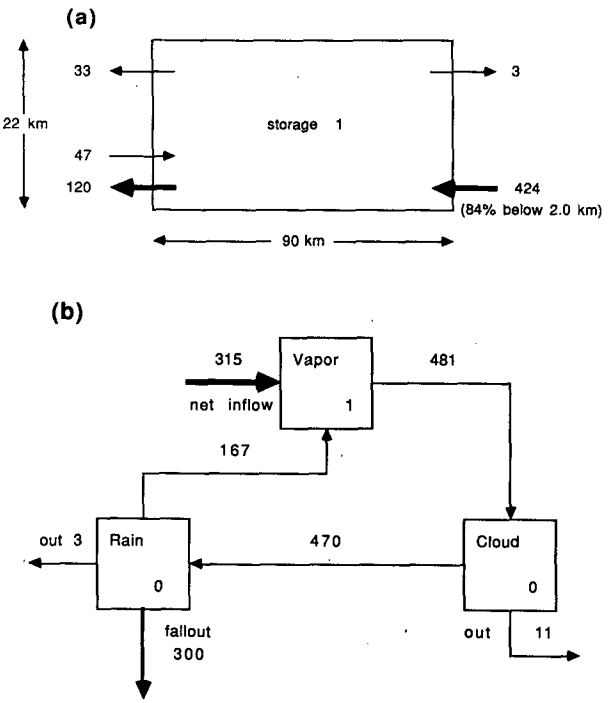

FIG. 14. Moisture fluxes (kg m^{-1} s^{-1}) for the subdomain. Part (a) shows average inflow and outflow rates of water vapor during the time-averaging period. Part (b) shows the moisture budget for the same time period. The values within the boxes represent the rate of storage; "out" refers to the net exchange with the surrounding domain.

which would be representative of the remote inflow environment. This increase can be explained by the enhanced inflow at midlevels on the front side which were induced by the storm (Fig. 13a). Vapor was exported from the subdomain at a rate of 156 kg m^{-1} s^{-1}; all but 2% of this occurred at the rear.

The net rate of inflow of water vapor into the subdomain was 315 kg m^{-1} s^{-1} of which 1 kg m^{-1} s^{-1} was retained in storage. This storage rate is small and dependent on the placement and width of the time-averaging window during the mature phase. Precipitation fell at an average rate of 300 kg m^{-1} s^{-1} and accounted for a very large portion of the net vapor influx. The concept of precipitation efficiency (PE) is an old one but there are numerous definitions and efficiency estimates vary widely as a result. In Table 1, which provides summary statistics for this simulation, the PE was estimated by dividing the total precipitation by the remote vapor inflow; this yielded an efficiency of about 79%.

If these values are multiplied by an assumed 20 km along-line segment, as has been done by Newton (1966) in his analysis of an Oklahoma squall line and others as well, the front side inflow and precipitation rates are 7.6 and 6.0 kt s^{-1}, respectively (kt ≡ kiloton). The figures are comparable to Newton's storm (8.8 and 4.7

TABLE 1. Numerical simulation statistics.

	Ice free	Full ice	No hail
Total precipitation (kg m^{-1} s^{-1})	300	329	279
rainfall	300	329	279
hailfall	—	0.2	—
Remote vapor inflow into storm (kg m^{-1} s^{-1})	382	434	434
Precipitation efficiency (%)	79	76	64
Maximum cooling behind gust front (K)	−11.5	−12.5	−11.7
Model gust front speed (m s^{-1})	14.0	15.6	15.6

kt s^{-1}), with the present case being considerably more efficient. However, little if any of the rain that fell could be considered stratiform. Figure 15 shows the average rainfall intensity over the two hour period relative to the leading edge of the storm. The rapid decrease of precipitation intensity away from the maximum indicates (along with Fig. 6) the absence of a trailing region of light precipitation.

Nor did a trailing region develop with time and the failure to produce this feature was the motivating factor for adding ice processes to the model microphysics. Figure 6 showed that during the storm's mature phase there was no indication that the *average* width of the precipitation area was increasing as the simulation progressed (i.e., long-term storage rates were virtually zero), despite the fact that production of new precipitation particles in the convective cells showed no signs of abating. Instead, an equilibrium width had been achieved.

The distance between the gust front and the region marked by subsidence warming at the rear provides a characteristic scale for the model storm's circulation. This scale was essentially determined by the ability of the storm to create condensed water particles and transport them rearward. Fig. 16 shows the time-averaged flux of these particles in the front-to-rear jet as a function of distance from the gust front. This transport can be seen to have decreased rapidly with distance from the region where the most intense cells (which were creating these particles) resided. Fallout from, and evaporation within, the front-to-rear jet contributed to depleting this transport, along with the deceleration of the jet with distance away from the leading edge. The former was very important since the large terminal velocity of raindrops prevented them from remaining in the front-to-rear jet for substantial distances after being created. While some amount of condensation was occurring in the older updrafts within the front-to-rear flow, the total amount of condensate produced away from the front of the storm was quite small in this case. This will be discussed in more detail later.

Some of the particles which fell from the jet evaporated in the subcloud layer, deepening the cold pool and counteracting the adiabatic warming produced by the downdraft layer. The downdraft which existed in this zone can be considered convective, due to its hor-

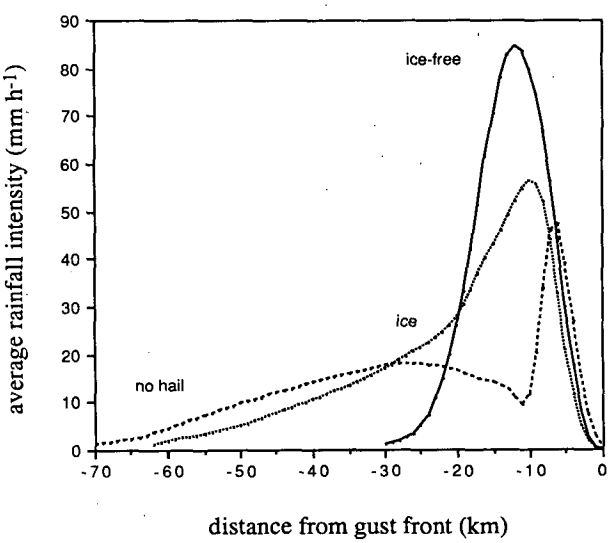

FIG. 15. Average rainfall intensity at the surface for the time-averaging period, relative to the surface gust front location. Curves show results for the ice-free run as well as for the full ice ("ice") model and no hail simulations to be presented later in this report. Negative distances are behind the front.

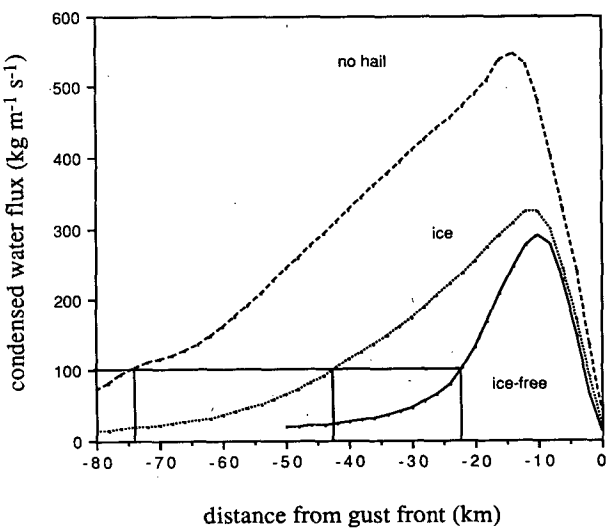

FIG. 16. As in Fig. 15, but for the time-averaged flux of condensed water (kg m^{-1} s^{-1}) in the front-to-rear jet with respect to distance behind the gust front. Vertical lines up from the horizontal axis represent the approximate locations of the forward boundary of the warm residence region for the storms. In each case, this boundary was taken to be where the rear inflow current descended into the surface cold pool.

izontal and temporal scales, and was very nearly saturated. Farther behind, where the fluxes were small, precipitation particles existed and evaporated in quantities insufficient to compensate for adiabatic effects. Beneath this highly unsaturated (and presumably mesoscale) downdraft, the cold pool was shallow and overlain by warmed, dried air (compare Figs. 11a and 11d). Precise separation of the model storm's downdraft layer into convective and mesoscale components is difficult since these drafts shared a common origin. They were produced beneath the aging cell updrafts near the leading edge and with time propagated rearward beneath them, becoming more and more unsaturated as the supply of rainwater from the updraft diminished.

c. *Sensitivity tests*

One must always be aware of the influence of artificial boundaries on the behavior of the model storm. A number of sensitivity tests have been made to gauge the impact of the boundary assumptions on the resulting storm structure. In particular, we were concerned that reflection of gravity waves produced by the model storm in the zone in between the fine and stretched grid, and off the rigid domain lid or the model stratosphere, were modulating or even causing either the short or long period oscillations of Fig. 6.

Reflection off the boundary between the fine and stretched grid regions was a concern because it is well known that a wave moving into a coarser mesh will tend to alias and/or reflect. To test this, another simulation was made in which 200 grid points were added to the fine grid region, which increased its width from 115 to 315 km. The stretched grid region was unaltered. While this modification greatly widened the fine grid region, the overall domain width was only slightly increased. Therefore, the effect of this change on the solution of the anelastic pressure equation should have been minimal. If either of the oscillations in Fig. 6 were modulated by gravity wave reflection off the stretched grid, then its effect should have been observable as a change in the form or timing of the cellular oscillation since with the wider fine grid area gravity waves would have a longer distance to travel before reflecting. However, the simulation made with the wider fine grid was virtually indistinguishable from the control run already presented and therefore we reason that this hypothesis can be rejected.

The rigid lid employed in this study is both the simplest to implement and the most common upper boundary condition in cloud models. However, a simulation made with the model top raised from 21.7 to 28 km was also found to be indistinguishable from the control run. The possibility that reflections were occurring in the stratospheric stable layer was the motivation for a test identical to the control run except that the constant temperature layer above 12.5 km was replaced with one having a lapse rate of 2 K km^{-1}. This simulation was also virtually identical to the control run.

Lowering the model top was found to affect the results. While the simulation made with the model top at 15.5 km still had major precipitation bursts at 33 min intervals, the precipitation field displayed an additional, even longer period oscillation than that which appeared in the control run. The structure of the longer oscillation was also different in a simulation initialized with a heat sink patterned after that used by TMM rather than a warm thermal. However, this model storm again produced major cells at 33 min intervals and yielded mature phase time-averaged fields nearly identical to those already presented.

The major difference between this run and the control is that the heat sink method, in providing a cold pool from the very start, allowed the storm to organize more quickly and enter its mature phase at an earlier time. The mature phases in the two runs were very similar, with the exception of the longer oscillation. The amplitude of this oscillation is actually quite small and Fig. 6 tends to exaggerate its importance. We conclude from these tests that the 33 min period is valid and the longer ones are spurious, with an unimportant influence on the model storm and our conclusions.

All of these simulations had in common a large horizontal domain, obtained by stretching the grid. Grid stretching was employed as a technique of moving the lateral boundaries from the immediate vicinity of the storm. This was done in order to minimize the influence such boundary conditions, both on the pressure as well as the momentum equations, can have on the model storm. Simulations made with small domains and unstretched horizontal grids showed considerable sensitivity to the choice of the gravity wave speed parameter c^* in the KW boundary condition. Relatively large values of c^* ($\sim$50 m s^{-1}) produced storm circulations which were qualitatively similar to the large domain runs in many respects, but details like precipitation patterns and amounts and the period and regularity of the cell regeneration process varied with the specific value of the parameter. Clark (1979) has criticized the usage of these perhaps unreasonably large values of c^*. However, while the storms produced in the large c^* experiments were more intense, they did not show any tendency towards becoming unstable, even over a very long period of time.

On the other hand, the employment of small values of c^* ($\sim$15 m s^{-1}) seriously impacted the ability of the model storm to survive through the production of new cells during the upshear tilting phase. These runs tended to have protracted periodically redeveloping phases, during which considerable subsidence warming was produced in the midlevel environment ahead of the storm. Subsidence warming in this region in the large c^* and large domain simulations was either absent or

confined to a narrow zone beneath the base of the forward anvil; the latter case can be seen in Fig. 11a. The extensive warming in the small c^* cases reduced the convective instability of the inflow environment and impacted the ability of air lifted over the gust front to achieve saturation. As a result, with time the small c^* model storms entered a decaying phase marked by the absence of significant cellular development rather than an extended, quasi-periodic mature phase.

Interestingly, further tests showed that the model storm was more sensitive to the value of c^* at the *upshear* rather than the downshear lateral boundary, even before the upshear tilting phase began. Since changing c^* at the boundaries in small domain simulations can have a significant impact on the general airflow throughout the domain, we prefer to use our large, stretched domain which puts the boundaries far from the storm and attempts, if crudely, to encompass the entire storm circulation.

5. Results—simulations with ice

The results of two numerical simulations made with the ice microphysics package activated are presented in this section. The first is a full ice model run which includes the entire LFO parameterization. Time-dependent and time-averaged model fields are described with emphasis placed on comparisons with the ice-free case. In the second simulation, hail was prevented from developing. Both the full ice model and no hail simulations were made with wider (315 km) fine grid regions and deeper (28 km) model domains, due to the more extensive dimensions achieved by these storms.

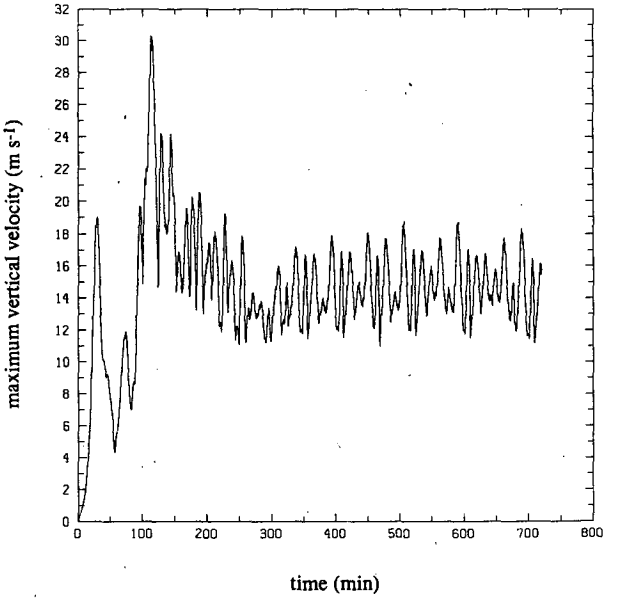

FIG. 17. As in Fig. 4 but for the full ice model run.

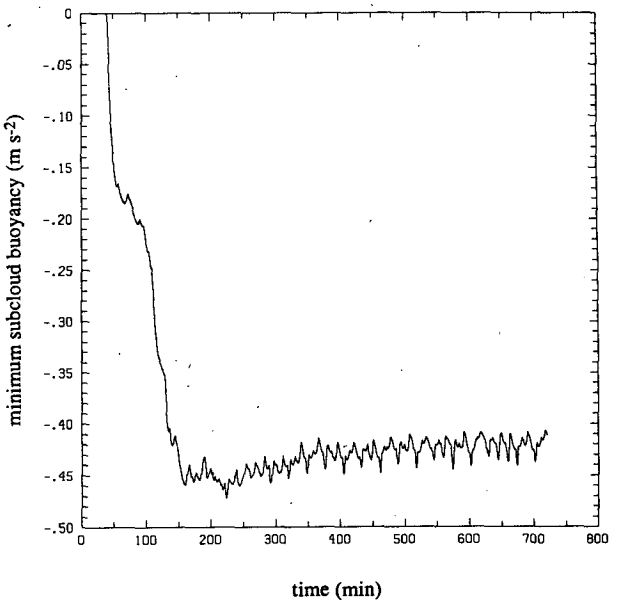

FIG. 18. As in Fig. 5 but for the full ice model run.

The results of sensitivity tests using the model design of the control simulation are also presented.

a. *Time-dependent behavior of the full ice model storm*

While the full ice model storm developed system-relative upshear tilt at about the same time into the simulation as the ice-free storm, it took longer to settle down into its mature phase. This can be seen in Figs. 17 and 18 which depict the time history of maximum vertical velocity and subcloud minimum buoyancy, respectively, over the 12 h period the simulation was run. The latter figure shows that this storm's cold pool was colder than in the ice-free case; maximum surface cooling averaged about −12.7 K (see Table 1). As a result, the model storm propagated more quickly, achieving a speed of 15.6 m s^{-1} during its mature phase. This is larger yet still comparable to the ice-free case; a similar situation was found by Yoshizaki (1986).

Figure 19 displays the total domain mass content for each of the five types of condensed water as a function of time. In the latter portion of the simulation, the total contents of cloud water, rain, hail and snow oscillated about relatively stable values while the ice crystal content possessed a distinct, long-term upward trend. This trend in the ice crystal field reflected the slow rearward (and upward) expansion of the high-level storm canopy. Note that, for example, increases in the hail content led increases for rain in time; we will show later that melting hail was the largest source of rain water in the model.

From Figs. 17, 18 and 19 it is judged that the mature phase of this storm was reached between 300 and 360

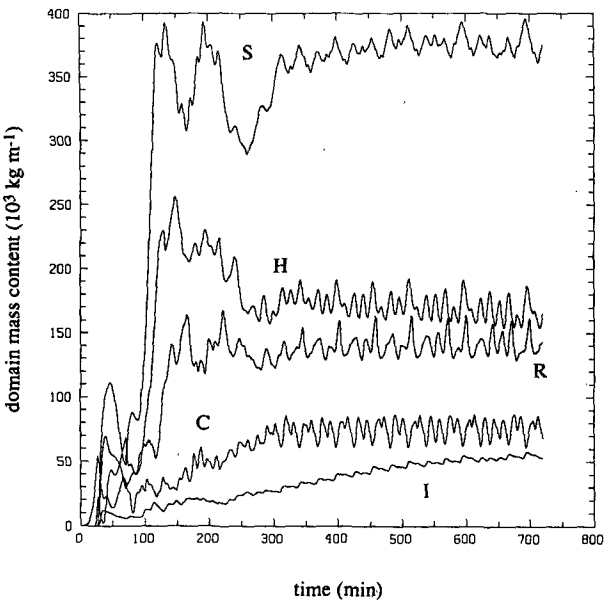

FIG. 19. As in Fig. 17 but showing the history of total domain mass contents (10^3 kg m^{-1}) for the various components of the full ice model microphysical parameterization. The letters "C," "R," "I," "S," "H" refer to cloud water, rain, ice crystals, snow and hail, respectively.

min. Figure 20 depicts the surface rainfall intensities recorded during this simulation, focusing on the period between 7 and 9 h. As in Fig. 6, this plot presents a 90 km section of the fine grid area. The boundaries of the stretched grid region are 81 and 145 km beyond the left and right sides of this figure, respectively.

It is clear that this storm was more horizontally extensive than in the ice-free run and produced a region of light precipitation at the rear (see Fig. 15). This trailing region was obviously fed by decaying cells which were born in the convective region. This is consistent with observations (e.g., Zipser 1969; Houze 1977) which determined that aging cells, the updrafts of which quickly decayed after their moisture supply was cut off, could transport much liquid and solid precipitation particles into the trailing region. While the canopy of the storm was slowly increasing in width with time, this figure shows that, like the ice-free case, the precipitating region had essentially reached an equilibrium width.

The surface precipitation pattern is similar to that of the ice-free case in that alternating strong and weak bursts were produced. The period between such pairs of cells in the figure is 28 min and an additional, longer period oscillation of 56 min is observable. The larger of the precipitation bursts in each pair were again associated with what we have termed major cells. As in the ice-free case, the secondary cells which appeared in between did not appear to be dynamically separate entities.

The major cells first appeared as discrete echoes above the gust front at a height of 3.6 km above the ground, just above the base state melting level. This height, lower than observed in the actual storm by SH1 (~5 km), is about the same as was found in the ice-free case (Fig. 7); in the latter, naturally, the melting level has no special significance. Figures 21a and 21b display the model simulated reflectivity and system-relative airflow structure, respectively, at 444 min into the simulation. The new echo, located above x = 77 km in the figure, later evolved into a major cell. It first appeared 2 min earlier and in its first 4 min intensified at a rate of about 5 dBZ min^{-1}. This growth rate appears reasonable when compared to the information of Chalon et al. (1976). While rain production through autoconversion of cloud water was undoubtedly important in achieving this intensification rate, the very first indication of the echo came from snow particles accreting cloud water in the new updraft. These crystals appear to have been detrained from the top of the mature cell immediately to the rear of the new echo and then settled out of the forward anvil. Therefore, in a sense, the mature cell has seeded the new cell.

The largest instantaneous rainfall intensity produced by the growing cell, 150 mm h^{-1}, occurred at 462 min, 18 min after the time of Fig. 21a. This value is substantially smaller than that of the major cells in the ice-free case. The time that the precipitation rate exceeded 100 mm h^{-1} from this cell was only 6 min; in the ice-free case, this time interval was 15 min.

The reflectivity maxima associated with the older

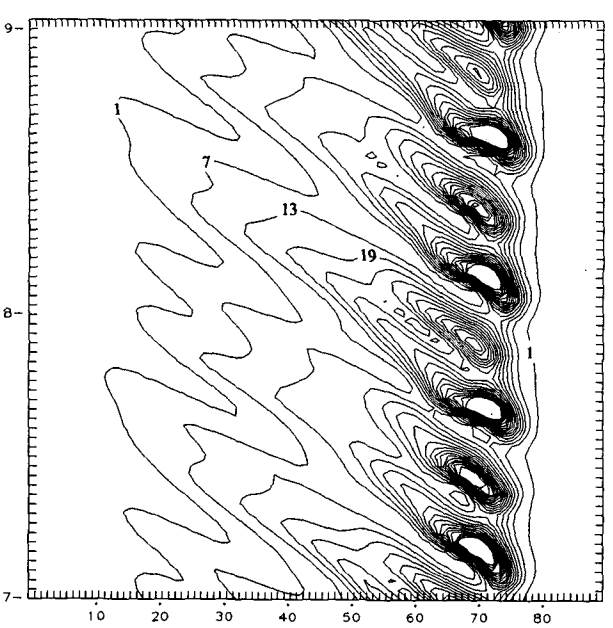

FIG. 20. As in Fig. 6 but for the full ice model run over the period between 7 and 9 h. The horizontal axis still shows a 90 km section of the fine grid region, but the frame of reference has been shifted to emphasize the trailing region. Domain speed is 15.6 m s^{-1}.

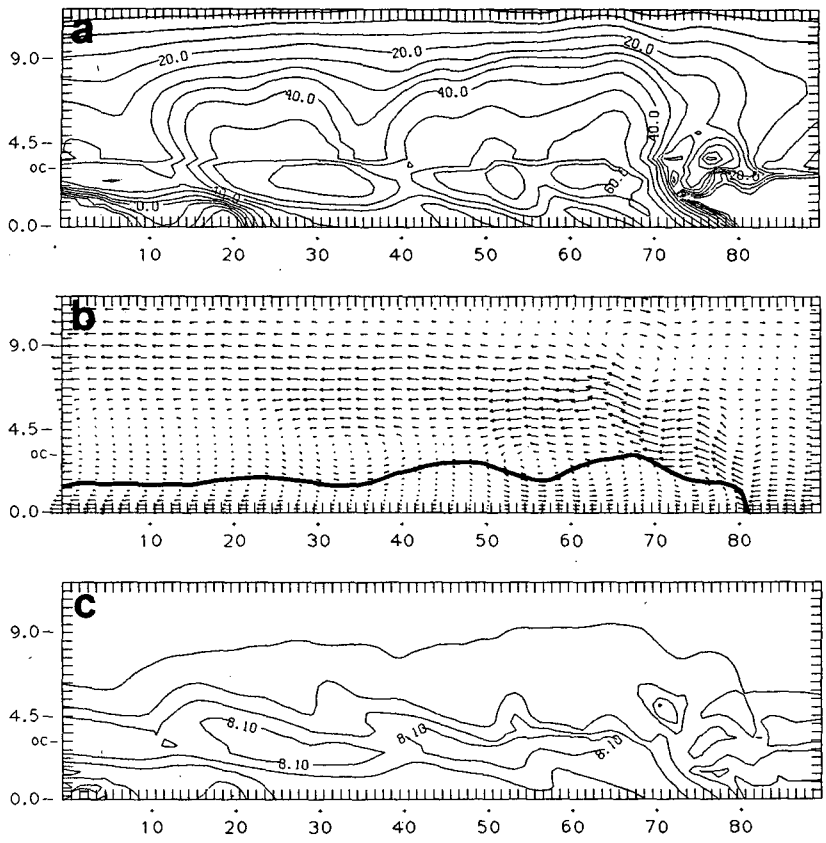

FIG. 21. Fields at 444 min into the full ice model simulation. (a) Radar reflectivity (contour interval 5 dBZ). (b) Airflow (vector scaling as in Fig. 8). (c) Mass weighted precipitation terminal velocity (2 m s^{-1}). Panels (d)–(g) depict the cloud water, rain, snow and hail fields, respectively, expressed as a mixing ratio (g kg^{-1}). Contour interval on these panels is 0.5 g kg^{-1}, beginning at 0.1 g kg^{-1}. On (f), the area in which ice crystal mixing ratios exceed 0.1 g kg^{-1} is stippled. Letters "0C" on the vertical axes show location of base state melting level.

cells in Fig. 21a were located at and below the melting level. These were caused by the superposition of rain water and ice particles, the latter essentially consisting of hail. In this figure, any ice residing beneath the melting level was assumed to be wet and able to reflect radar waves more efficiently and this was handled by taking α in (1) to be one. The result of this was the creation of a high reflectivity layer suggestive of a bright band.

The large thickness of this band was due in part to the large terminal velocity of hail which allowed some of these particles to survive even well below the melting level. It should be noted that while the reflectivity enhancement augmented the bright band it did not itself create this feature. Figure 21c depicts the spatial distribution of mass weighted fallspeeds predicted by the model; the large values near the melting level (>8 m s^{-1}) reflect the presence of hail. Hailstones have larger terminal velocities than raindrops and therefore reflecting particles tended to accumulate in the zone where hail melts into rain.

Figures 21d–g depict the distributions of water substances at 444 min. Cloud water (Fig. 21d) can be seen to have been confined to the region which encompassed the new and mature updraft; behind this region the cloud above the melting level was almost entirely glaciated. Cloud ice concentrations (stippled area in Fig. 21f) were small and chiefly confined to the upper troposphere and lower stratosphere; at lower levels, only small amounts of cloud ice were formed and those crystals did not survive very long before being collected. A comparison between the rain and hail fields (Figs. 21e and 21g) demonstrates that the former was primarily supplied by the latter. At the rear, it can be seen that aggregation of snow crystals in the oldest cells formed hailstones which fell swiftly to the melting level; Lord et al. (1984) reported a similar experience. The conversion of snow crystals into hailstones is perhaps a crude replication of the observed increase in the size and density of ice particles approaching the melting level (e.g., Stewart et al. 1984) although the reason why they accumulate there is probably not very realistic.

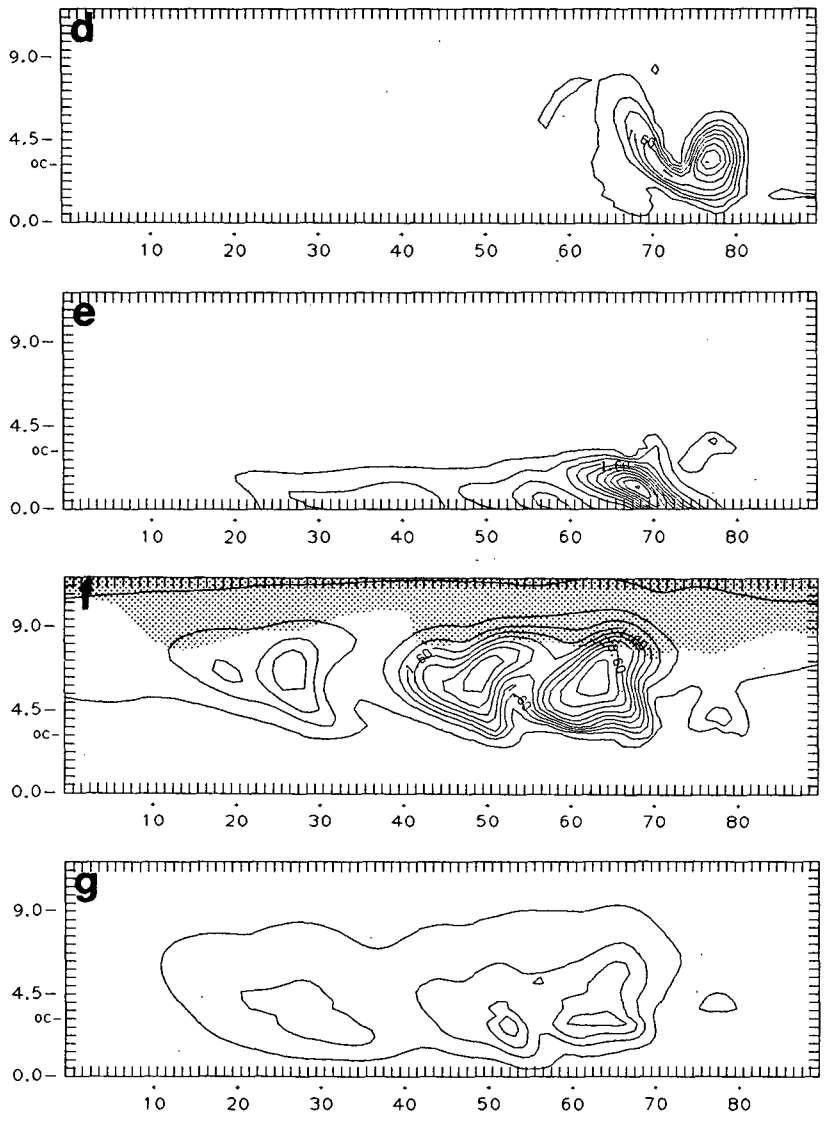

FIG. 21. (*Continued*)

b. Time-averaged structure of the full ice model storm

Figure 22 shows the time-averaged structure for the ice model storm, again for a period during the mature phase encompassing an integral number of cellular developments. The overall basic structure of this storm resembles that of the ice-free run presented previously, the major difference being the larger scale of the features. The increase in scale can be attributed to the enhanced water transport in the front-to-rear jet in this storm (Fig. 16). The larger fluxes at the rear of the ice model storm provided the precipitation particles which were needed to create the trailing region of light rain.

The enhancement in the rearward precipitation flux in this run was principally due to the fact that in the ice model little rain existed above the melting level at any one time or location in the model storm. Rain that was produced above this level collided with snow crystals or hailstones and resulted in the augmentation of one of those fields. Due to its rapid fallspeed, hail produced in the front-to-rear jet fell out of the cloud quickly enough so that its impact on the snow field was smaller than that of rain on the cloud water field in the ice-free case. The net effect was that more condensed water, most of it in the form of slowly falling snow crystals, was carried farther rearward in the front-to-rear flow. The greater spread of the cooling due to evaporation, sublimation and melting of these precipitation particles helped keep the downdraft layer moist over a greater area, allowing the storm to widen in extent.

Figure 23 presents the moisture budget for this sim-

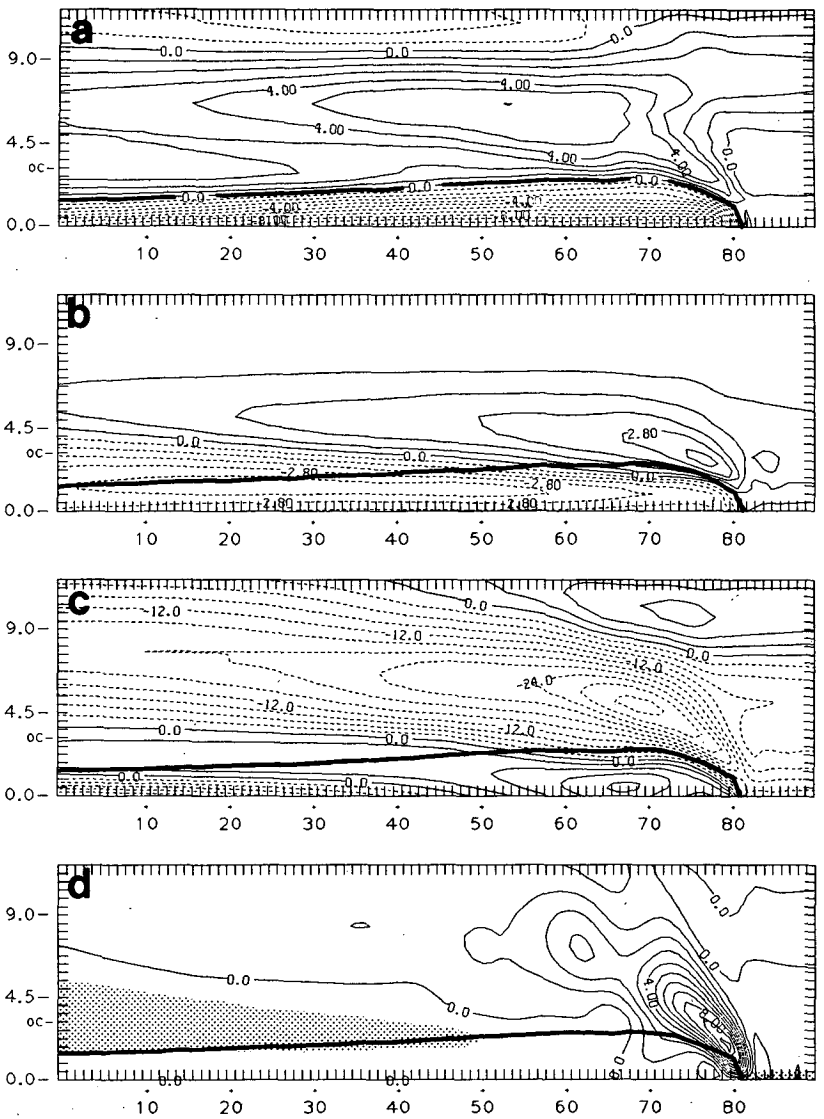

FIG. 22. Time-averaged fields for the full ice model run. Format same as in Fig. 11. Again depicted are (a) potential temperature deviation from the initial state; (b) water vapor mixing ratio deviation from the initial state; (c) system-relative horizontal velocity; (d) vertical velocity; (e) perturbation pressure; (f) airflow pattern; (g) radar reflectivity and (h) equivalent potential temperature. Units and contour intervals same as in Fig. 11. Letters "0C" show location of base state melting level.

ulation during the time-averaging period. This budget was calculated for the entire 315 km fine grid region which completely enclosed the condensate produced by the storm. Where there was more than one process acting between two water substances, the net transfer rate is given. As an example, the small exchange between rain and snow indicates that accretion of rain by snow was very nearly balanced by the loss of snow to rain through melting.

Precipitation fell at a rate of 329 kg m^{-1} s^{-1} of which only an insignificant amount (0.2 kg m^{-1} s^{-1}) was in the form of hail. This total was slightly greater than the 300 kg m^{-1} s^{-1} rate recorded for the ice-free simulation but the precipitation in this case was far more spread out (Fig. 15). Also, since the ice model storm propagated more quickly, the remote system-relative water vapor inflow rate was larger (434 kg m^{-1} s^{-1}). Therefore, its precipitation efficiency (76%) was slightly smaller than in the ice-free case.

The major path in Fig. 23 is from water vapor to cloud water to snow to hail to rain water. Melting hail was the primary source of rain production, accounting

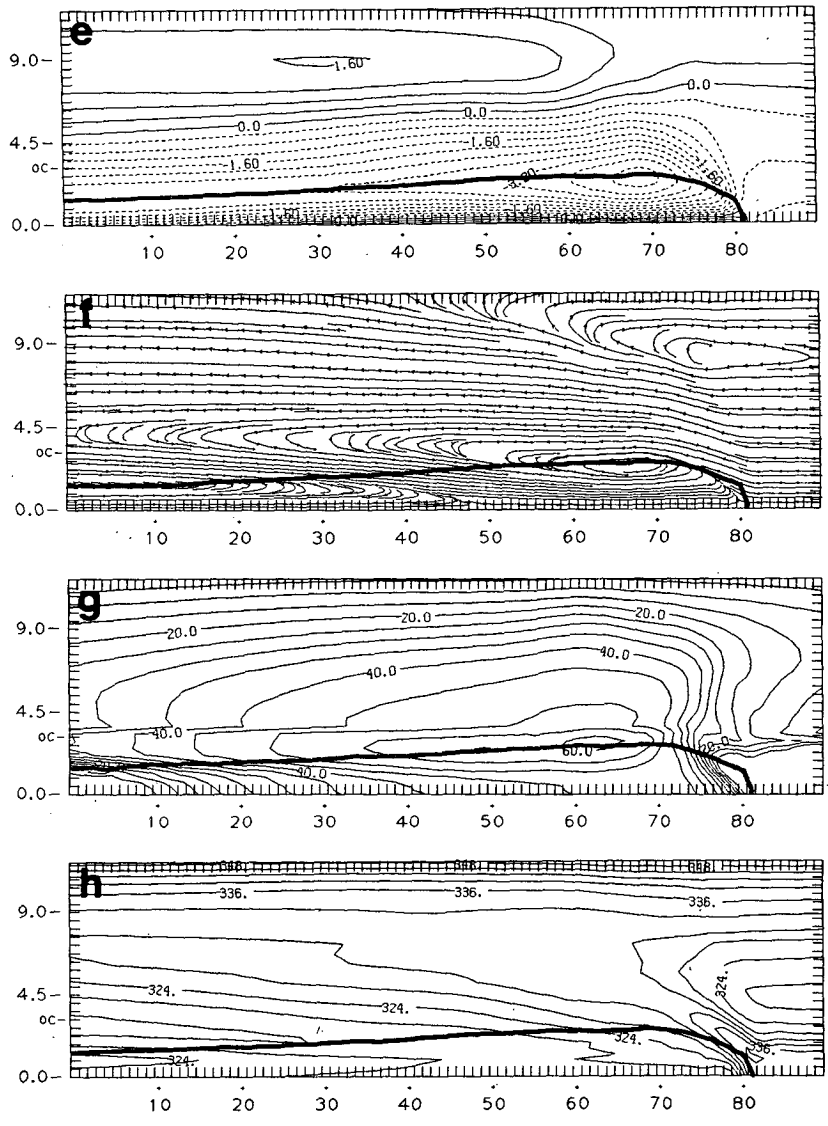

FIG. 22. (*Continued*)

for 97% of the rain produced through the melting process. Also, it can be seen that the role of hail was to scavenge the snow field. This must have been a controlling factor in determining the storm's precipitation efficiency and ultimate equilibrium width. Microphysical modifications affecting the production of snow relative to hail should alter the PE and the horizontal scale of the convective region significantly.

c. A no hail simulation

To test the impact of the hail portion of the parameterization on the model storm's structure another simulation was performed deleting the processes which create hail. This simulation will be discussed briefly in this section and compared to the full ice model case. As in the ice-free and full ice model cases, this no hail model storm reached a long-lasting mature phase marked by quasi-regular production of new cells; in this case, however, the storm took even longer to settle down. Once it did, it achieved a propagation speed of 15.6 m s^{-1}, the same as in the full ice model simulation (Table 1).

Figure 24 shows the rainfall pattern produced by this storm between 9 and 11 h. The time period between large precipitation bursts associated with major cells was approximately 30 min, about the same as in the previous two simulations, and a secondary cell also appeared in each repeat cycle. In this case, however, the major bursts were of smaller intensity and confined to a narrower region behind the gust front. As in the full ice model case, a zone of lighter precipitation ex-

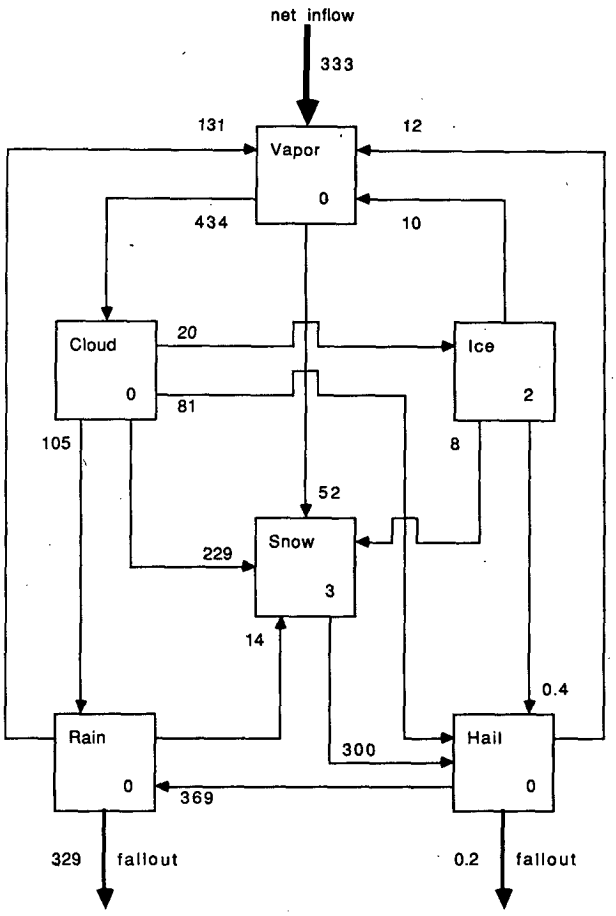

FIG. 23. As in Fig. 14b but for the full ice model storm. This budget was calculated for the entire 315 km fine grid region which totally enclosed the condensed water produced by this storm.

isted in the trailing portion of the storm. In this case, however, the extensive, lighter precipitation region was separated from the more intense rainfall near the gust front by a zone in which the rainfall intensity was consistently very small. This zone, which was located about 10 km behind the gust front, can be detected in Fig. 24 above $x = 70$ and in Fig. 15 as well.

Time-averaged fields for a period during the mature phase are presented in Fig. 25. It can be seen that the basic features were yet again increased in scale. Temperatures within the cloud near the leading edge were warmer (Fig. 25a) and the averaged system-relative horizontal winds in both the front-to-rear jet and the rear inflow current were stronger (Fig. 25c) than in previous simulations. The subsidence region resided even farther from the leading edge; its forward boundary can be seen at the far left side of Fig. 25a. Between this region and the leading edge, the cold pool was extremely deep; its top (~3.2 km) approximately coincided with the base state melting level between $x = 25$ and 70 in Fig. 25a. The subcloud layer was deepened because snow melted closer to the melting level that did hail in the full ice model case. This was due in part to the small fallspeed of snow crystals.

Very large quantities of snow were produced and carried rearward in the front-to-rear jet since there was no hail to deplete the snow field (see Fig. 16). This enhanced rearward flux, almost exclusively consisting of slowly falling snow particles, allowed the precipitation to be more spread out. The total domain precipitation rate was 279 kg m^{-1} s^{-1} during the mature phase, smaller than for the full ice model storm. Since the propagation speed (and thus the remote vapor inflow rate) was the same, this storm's precipitation efficiency was reduced to 64%.

Again, the warm, dry subsidence region resided where the rearward precipitation flux had become small (Fig. 16). The vertical lines on the figure mark the location of the forward boundary of the subsidence region for the simulations, taken in each case to be the point where the rear inflow current descended into the cold pool. The figure suggests that this region existed in each case where the rearward flux was reduced to below approximately 100 kg m^{-1} s^{-1}.

This simulation also produced a horizontally aligned echo in its time-averaged reflectivity field (Fig. 25g) which resided just below the melting level. Rainfall at the surface beneath this bright band was fairly uniform in the horizontal (Fig. 15). This precipitation did fall out of the decaying cells as they traveled rearward, although this is less clear in Fig. 24 than it was in the full ice model storm case (Fig. 20). In this case, the band was substantially shallower and centered closer

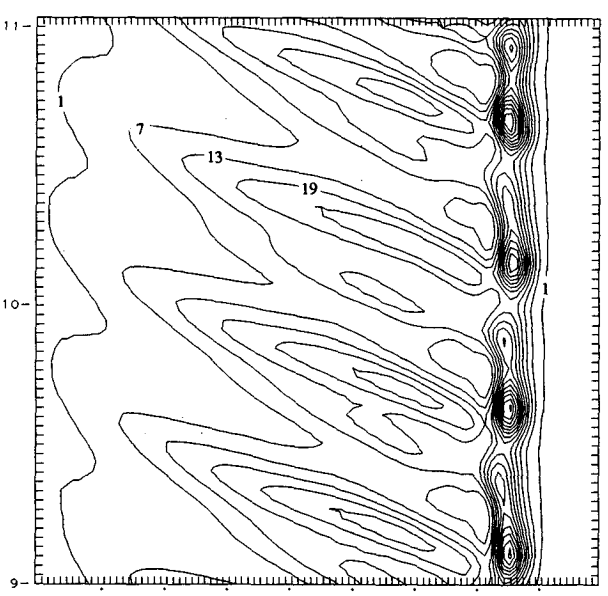

FIG. 24. As in Fig. 20, but for the no hail simulation between 9 and 11 h. Domain speed is 15.6 m s^{-1}.

to the melting level than it was in the full ice model case, and was produced by the superposition of snow crystals and rain water. While the accumulation of reflecting particles in the melting zone was again important in creating this feature, the reasons behind the accumulation were quite different in this case. It can be seen in Fig. 25c that the system-relative airflow in the zone the banded echo was embedded in was quite stagnant and snow crystals which happened to enter this zone tended to become trapped due to their small terminal velocities.

The averaged vertical velocity field (Fig. 25d) shows that the convective updraft was more concentrated near the leading edge in this case than in the others. Individual cell updrafts decayed very quickly as they traveled rearward, perhaps due to increased water loading owing to the large amounts of snow they bore. The figure suggests that the upward motion in the anvil at the rear was separate from that at the system's leading edge. In the previous simulations, the trailing anvil updraft was fed (at least in part) by old, weakened convective cells. In this case, we can note the obvious correlation between the base of this upward motion in the anvil and the maximum velocity axis of the front-to-rear jet, suggesting that convergence in the decelerating airflow was contributing to its presence. This occurred in the ice-free and full ice model cases as well, although it was obvious only much farther behind the leading edge in those model storms.

d. Sensitivity tests

Because the ice model storms achieved greater horizontal width, an expanded fine grid region was used in both of these simulations. This was done because sensitivity tests showed that increasing the width of the fine grid did affect the time-dependent results somewhat. Since the expanding grid acts to dissipate the convection, as much of the strongly perturbed airflow as possible should reside within the fine grid region. The 315 km fine grid width used was more that sufficient to contain both the portion of the storm with significant horizontal gradients and all of the condensate produced by the convection in the ice model simulations.

The height of the domain top was also increased for these runs. Simulations with lower domain tops tended to have more, higher amplitude long period oscillations superimposed on the same basic precipitation pattern; this was true in the ice-free case as well. However, while the precipitation pattern produced by the ice-free case appeared to be essentially fixed, those produced by the ice models tended to shift in appearance somewhat with time. In the full ice model case, the shift occurred at about 10 h; evidence for this can be seen in Figs. 17 and 19. While the essential short period characteristics of the pattern remained the same after this time, the longer period components looked more like they did in a simulation which employed the shallower domain depth (21.7 km) used in the ice-free case.

The greater sensitivity to the domain depth in the ice models may be due to the presence of ice crystals in the stratosphere and upper troposphere. Little cloud water was able to reach up that far in the ice-free storm but the bulk of the cloud ice which survived for any length of time resided there. In the full ice model case, part of the general upward trend in cloud ice content with time (Fig. 19) was due to crystals reaching farther into the model stratosphere. In fact, we have found that changing the moisture profile at upper levels was sufficient to modify the longer period components of the precipitation oscillation in the full ice model storm.

These different oscillations and patterns, however, were not obviously functions of the cloud ice content. Nor was there any evidence of spatial or temporal instabilities in the moisture distributions. Indeed, the time-averaged fields for different periods of time possessing different long period oscillations were virtually identical. This shows that, on the broadest scales, nothing had really changed. Therefore, we again conclude that the smaller amplitude, longer period variations are spurious and unimportant.

We have found that the ice model, with its many externally set coefficients such as MP intercepts, autoconversion thresholds, collection efficiencies and terminal velocity parameters, is rather sensitive to alterations in these values. While we were able to alter the total precipitation, rainfall and hailfall intensities, precipitation efficiencies and rainfall patterns produced by the model storms by altering these parameters, we have found that the broad features of the convective regions of these simulations as manifested in the airflow and multicellular structure were substantially similar among the simulations. While the greater rearward spread of precipitating particles realized in the ice simulations was responsible for the achievement of features more realistic in scale and appearance, it did not appear to make a major impact on the underlying dynamics of the model storm.

6. Discussion

a. Lack of decaying phase in the model storms

Since in a large domain simulation the characteristics of the remote inflow environment were essentially unchanged with time, the mature model storm was continually propagating into the same favorable environment which allowed it to reach the mature phase in the first place. This appears to explain why the model storms presented herein do not experience a dissipating stage, at least not within a reasonable period of time. Instead, the model storms continued to produce new cells and semiregular precipitation patterns throughout

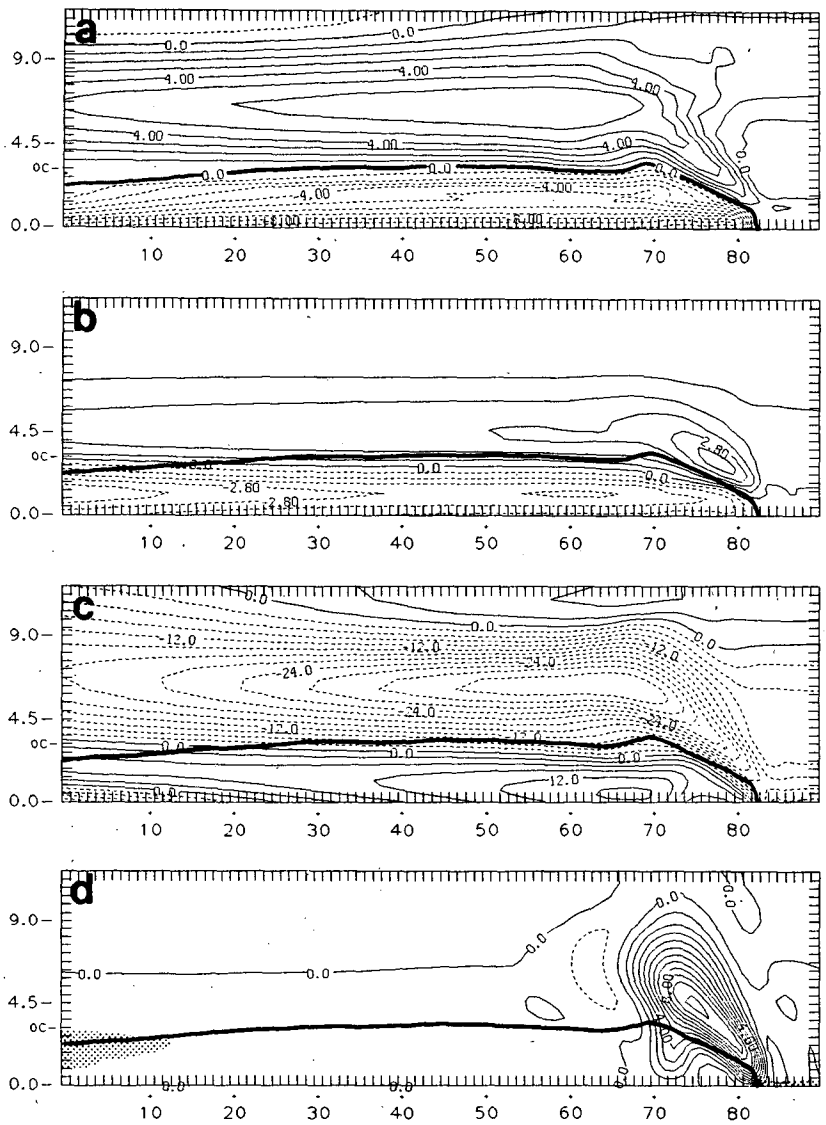

FIG. 25. Time-averaged fields for the no hail simulation. Format same as in Fig. 11. Again depicted are (a) potential temperature deviation from the initial state; (b) water vapor mixing ratio deviation from the initial state; (c) system-relative horizontal velocity; (d) vertical velocity; (e) perturbation pressure; (f) airflow pattern; (g) radar reflectivity and (h) equivalent potential temperature. Units and contour intervals same as in Fig. 11. Letters "0C" show location of base state melting level.

the integration which, for the ice model cases, was 12 h. This continued as long as the storm was not allowed to enter the stretched grid area ahead of it.

Squall lines do have definite life cycles in nature, and there is some disagreement about the mechanisms that force their decay. Drying of the environment ahead of the storm by compensating downdrafts has been postulated by Feteris (1961). No significant drying occurred out ahead of the storm in our simulations, in part because the large domain used allowed compensating downdrafts to spread out. Lateral boundary conditions cannot be completely open in the sense that they allow subsidence to occur outside of the domain. Yet even model storms within small physical domains did not decay when the lateral boundaries were appropriately handled. The decaying phase which resulted when the boundaries were inappropriately handled may resemble that of a squall line in some respects, but one needs to demonstrate that the decay was not numerically forced.

In any case, to adversely affect the storm through drying, the compensating downdrafts would have to

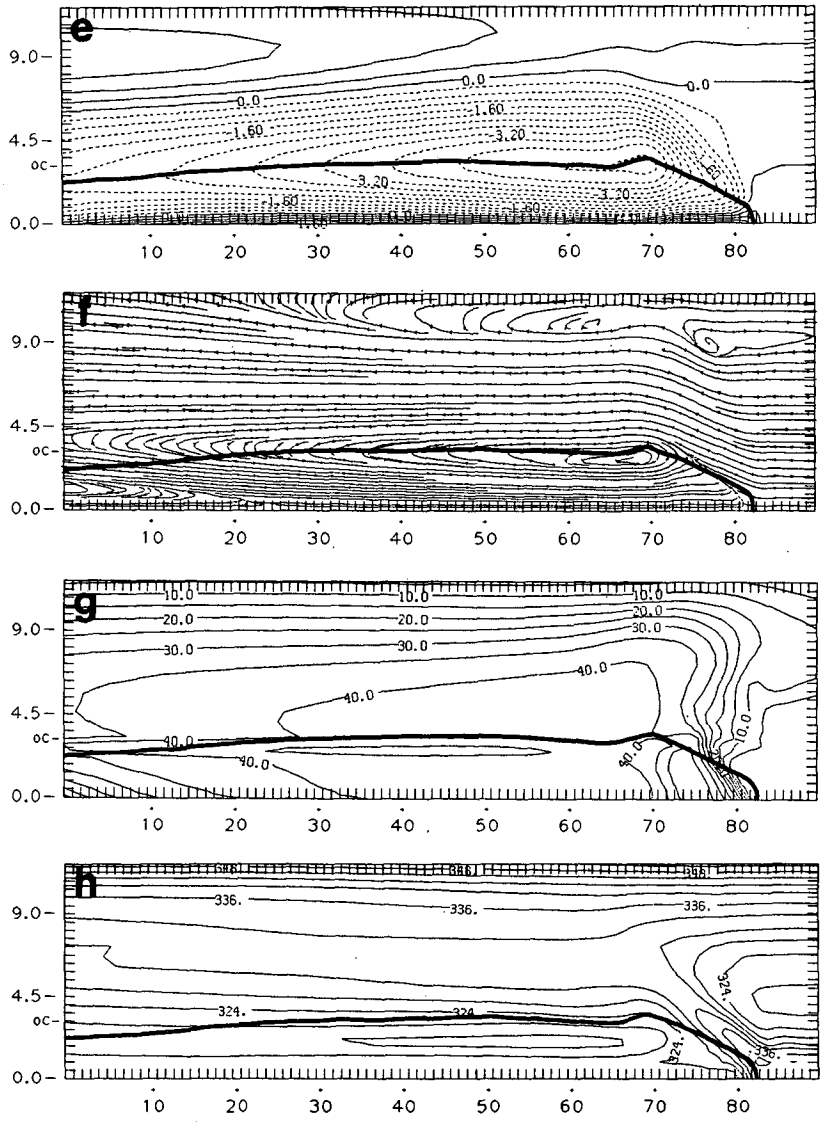

FIG. 25. (*Continued*)

reach down to the surface to alter the inflowing moisture which was drawn primarily from low levels. This is not likely to occur, as was pointed out by Wade and Foote (1982) who studied a case in which both drying and interference between cells along the line contributed to decay. According to OL, the case being considered here may have dissipated due to unfavorable moisture convergence into the storm area associated with winds directed *along* the line; this component has been neglected in these strictly two-dimensional simulations.

The above suggests large scale influences and speculation along these lines was advanced by Leary and Houze (1979). Certainly, storms do not exist in horizontally homogeneous, time-invariant environments such as that used in the model. In reality, storms may propagate from a favorable area into one which has been modified by larger scale motions, diurnal effects or other forces. Also, because of the model storm's rear inflow feature, the structure of the pre-storm environment behind the line could also have some impact on the storm's life cycle and ability to survive.

b. The appearance of the secondary cells

The mature phase of each model storm presented in this report was marked by essentially repetitive behavior with respect to cell production. In each case, a repeat cycle consisting of two cells, one major and one secondary (or minor), was evident, although details of

the cycle varied among the cases. As noted earlier, the major cells appeared above the gust front as new, discrete entities with respect to reflectivity and updraft while the secondary cells which followed them did not appear to be truly distinct dynamically. Rather, they appeared to be perturbations superimposed on the already existing updraft established by the previous major cell.

This represents a departure from the classic multicell model in which each cell is essentially disassociated from those previously existing and may be more similar to the "weak evolution" idea of Foote and Frank (1983). They examined a storm that was marked by a sequence of individual cells which appeared to be but small perturbations on, or periodic reintensifications of, an already established updraft. They termed this "weak evolution" to contrast this behavior with the "strong evolution" of the classic multicell model.

We have found, in simulations not reported herein, that the production of secondary cells disappeared when the low-level wind shear was decreased. When wind profiles with stronger shear were employed, no discrete major cells were produced at all. Rather, all cells were deemed to be secondary and the simulated storm fit the description of the weak evolution model. Thus, our present case appears to reside in a transition region between the strongly and weakly evolving modes because it does not fit either category very well. These wind shear tests will be described in a future report.

The timing between successive cells and the length of each repeat cycle can also be modified by manipulating the model microphysical and diffusional parameters. Enhanced mixing within the cloud tended to hold the cells together, increasing the period. A simulation made with the full ice model in which the cloud-to-rain autoconversion process was deactivated underwent a period in which two secondary cells followed each major cell over a repeat cycle of about 42 min. The deleted process was relatively minor compared to others in the parameterization in the full ice model simulation described earlier, in part since the region of the storm in which it was active was rather small. However, it could control or influence rainwater production in the new cell and thereby, perhaps through downdrafts, impact the character of the oscillation. Interestingly, although the precipitation pattern produced by this storm differed in appearance from that presented in Fig. 20, the time-averaged fields for this case were very nearly the same as those presented in Fig. 22. This suggests that the most basic characteristics of these model storms were the same. Also note that the addition of a secondary cell to the repeat cycle coincided with its lengthening from 28 to 42 min with the result that the average period between cell developments, whether major or secondary, was unchanged with the deletion of the autoconversion process. This is an oversimplification because the component cells of a repeat cycle tended not to be equally spaced in time, but does point to something which should be given closer examination in the future.

Recall that DMS required a rearward jet in the initial wind profile to produce a clearly multicellular storm whereas ours did not. The numerical simulations of TMM have demonstrated that the wind shear through midlevels can have an impact on determining storm type and the characteristics of individual cells. For their simulations, DMS used a tropical sounding which possessed less instability and, because it was more humid at low levels, produced a less intense subcloud outflow. The pressure forces, both buoyant and dynamic, associated with the lifting and rearward transport of the inflowing air were certainly much larger in our case and perhaps this is the reason why a midlevel jet in the base state was not required to impel the individual cells rearward. Weisman and Klemp (1982) demonstrated in their three-dimensional simulations the validity of the idea that both the buoyancy and the shear contributed to determining storm type; therefore, one cannot be considered without the other. It is possible that further reconciliation between our results and those of DMS can be accomplished within the framework of the recent theory postulated by Rotunno et al. (1988), particularly if the role of midlevel winds are dealt with in a more explicit fashion.

c. Model storm structure in the trailing region

While the ice model storms possessed some features in their trailing regions which were somewhat stratiform in appearance, they deserve closer examination. None of the storms clearly developed a transition zone like that observed by SH1 and SH2 between the convective and stratiform regions in the actual storm. SH2 found this zone, characterized by relatively small reflectivities at low levels, to be associated mainly with a layer of relatively intense downward motion. The no hail simulation may have come closest to producing this feature, if the rainfall and low-level reflectivity minima about 10 km behind the gust front (see Figs. 15 and 25g) can be considered such a zone. This zone separated the intense precipitation zone near the leading edge from the lighter, more uniform rainfall which occurred beneath the "bright band" echo (Fig. 25g) which is usually identified with stratiform regions. However, then the convective zone would be very narrow and, in any case, the airflow within the subcloud region may have played a major role in concentrating the precipitation close to the leading edge.

We have already noted that the condensate produced in the convective cells and carried rearward in the front-to-rear jet was of primary importance in establishing the trailing region of light rain in the ice model simulations. Some recent observational and numerical studies, however, have focused on the production of

condensation within the high-level mesoscale updraft at the rear itself. For example, Gamache and Houze (1983) studied a tropical line and found that approximately 25%–40% of the condensate in the stratiform cloud was produced in situ by the mesoscale updraft. Rutledge's (1986) simulations of this tropical case have also stressed that some of the precipitation far behind the storm had to have been initiated from condensation originating in this updraft.

Figure 26 presents the spatial distribution of the time-averaged condensation rate for the ice model simulation without hail. Condensation here includes both the creation of new cloud droplets from vapor as well as the deposition of vapor onto previously existing snow crystals. The large values associated with the convective cells, the largest of which was 6.6 kg m^{-1} s^{-1}, have been deleted in order to focus on the much smaller rates in the trailing region. Not surprisingly, the contours in the deleted zone corresponded closely in density and orientation to those of the updraft velocity in Fig. 25d.

The rates in the front-to-rear jet at the rear were locally quite small, with a maximum of about 0.18 kg m^{-1} s^{-1}. However, since this condensation process acted over an areally extensive zone, the total production in this zone did accumulate to a non-negligible amount. Comparison of this field with Fig. 25c shows that condensation production was well correlated with vapor convergence in the decelerating front-to-rear airflow. Direct comparison between these data and those of Gamache and Houze (1983), for example, entails having to choose a definite boundary between the convective and anvil regions. Still, we can note that of the total condensate production in the front-to-rear flow, 13% was produced rearward of $x = 60$ in Fig. 26 with 10% behind $x = 50$.

This production appears to compensate for fallout to a degree sufficient to keep horizontal reflectivity gradients small in the updraft region (e.g. 30 dBZ contour in Fig. 25g). Beneath the base of the updraft, evaporation, sublimation and fallout were acting to clear that area of condensed particles, depleting the total rearward transport in the front-to-rear jet. The condensation rates in the trailing updraft region for the full ice model case, as well as the ice-free case, were smaller than in this simulation and also less horizontally extensive. Also, neither possessed a zone of condensation within their cold air pools like that which can be seen in Fig. 26; relative humidities there were at or near 100% over a very wide and deep zone in this case.

If these rates and percentages are small, then two factors may be contributing to limiting condensation in the trailing region. Obviously, the addition of the third dimension could allow the development of more realistic airflows, enhancing condensation at the rear in zones marked by mass and moisture convergence. Also, the LFO parameterization does not have an explicit transfer process between vapor and cloud ice. Instead, all such ice is created from cloud water, with the result that the formation of new cloud ice in the mesoscale updraft at the rear of the storm requires local supersaturation with respect to water. Rutledge and Hobbs (1983) and Lord et al. (1984), two studies which used parameterizations similar to (or based on) that of LFO, have included vapor-to-cloud ice processes. The latter directly included ice in their saturation adjustment process to enhance ice crystal concentrations. Preliminary tests with a saturation adjustment process modified to include ice showed that condensation rates could be increased by about 25% in the high-level updraft; however, other aspects of the model storm's character were but little changed.

7. Summary

These simulations represented attempts to numerically replicate the basic features of the Smull–Houze conceptual model with a two-dimensional, anelastic cloud model, using initial conditions adapted from the 22 May 1976 Oklahoma line. Simulations made with and without including ice phase processes were presented. These model storms were similar in that they organized themselves into long-lasting mature states marked by multicellular behavior, as was observed in

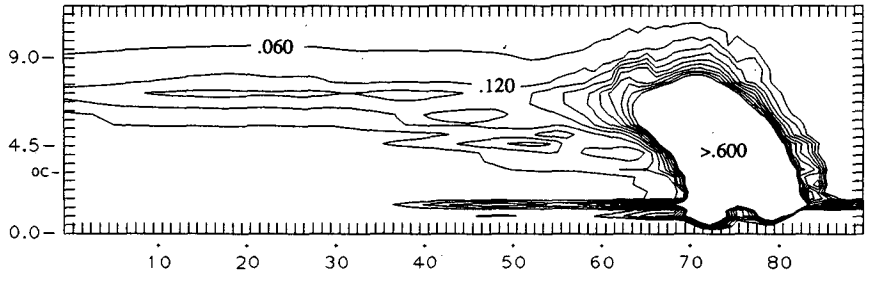

FIG. 26. Time-averaged total condensation rate for the no hail simulation. Contour interval 0.06 kg m^{-1} s^{-1}. Contours above 0.6 kg m^{-1} s^{-1} have been deleted in order to emphasize the trailing region.

the actual storm. Air was ingested into each model storm primarily from low levels and accelerated rearward and upward over a surface pool of evaporatively chilled air. This airflow gave the main storm updraft a relative rearward (upshear) tilt with height, consistent with the observations.

Beneath this front-to-rear flow at high levels, a rear inflow current developed. This feature has been noted in many actual and simulated storms in the past. In each case, the inflow current resided above the shallow rear branch of the cold pool in the warm and dry air of the trailing region and descended into the pool as it progressed towards the front of the storm. We have been able to attribute the location of this feature to large-scale pressure gradients but note that the mass continuity constraints of the two-dimensional model can exaggerate its intensity. The role of the inflow current deserves further investigation since, as it feeds dry air into the subcloud cold pool, it may be able to influence the storm by enhancing evaporation of rainwater in the pool which could, in turn, affect the speed of movement of the storm as well as other factors.

The storm survived through the production of new cells at the leading edge of the storm, over the system's gust front, the forward boundary of the cold pool. This production proceeded in a quite regular, although somewhat different, manner in each case. Thus, each of the model storms appear to have achieved a very long-lasting, quasi-equilibrium state. The lack of decay in the model storms was attributed, at least in part, to the storm's inability to greatly after the favorable and essentially time-invariant environmental conditions far ahead of it, a consequence of the model design.

Sensitivity tests were conducted to test the validity of the quasi-equilibrium behavior. These tests revealed that while the smaller amplitude, longer period elements of the oscillatory cell generation process were spurious, the larger amplitude, shorter period ($\sim$30 min) components which dominated the simulations appear to be reasonable. Each short period repeat cycle involved the production of two cells, one major and the other secondary or minor. The former appeared as a discrete, new updraft at the front of the storm while the latter was generated farther to the rear and was not clearly separated from the major cell it followed. This behavior deviates from the classic multicell model and was discussed with reference to the "weak evolution" model of Foote and Frank (1983).

The individual cells traversed rearward relative to the front as they aged, transporting condensed water created in their updrafts into the trailing portion of the storm. This rearward flux of particles was enhanced by including ice, particularly low density snow. Ice inclusion also resulted in the production of model estimated radar reflectivity fields which were more realistic in appearance and allowed the establishment of a trailing region of lighter rainfall. The latter was due in part to the less rapid depletion of the rearward condensate flux through fallout. The ice model storms also propagated more quickly than did the ice-free case, probably due to the contribution of melting ice particles in increasing the coldness and depth of the subcloud cold pool.

The general features of the model storms were quite similar among the runs, while the scales of these features were essentially controlled by the intensity of the rearward flux of condensate. The structure of each model storm in the mature phase was investigated by averaging model predicted fields across time in a system-relative manner over an integral number of repeat cycles. This technique smoothed out the transient components of the circulation associated with the time-dependent cells and revealed its basic, underlying character.

The major limitations of the model are its two-dimensionality and the lack of significant production of condensate in the high-level updraft at the rear, two factors which may be at least partially related. Additional tests need to be performed to gauge the impact of the model's geometry on the simulated storm structure.

Acknowledgments. The authors wish to thank Margaret LeMone and Bradley F. Smull for their valuable comments. Critical reviews by Morris Weisman, Mitchell Moncrieff and the journal reviewers also helped us improve the manuscript. This research was supported by the National Science Foundation under NSF Grants ATM84-15222 and ATM87-00778. The model simulations were made using the Cray X-MP computers of the National Center for Atmospheric Research, which is sponsored by the National Science Foundation, and the National Center for Supercomputing Applications at the University of Illinois at Urbana–Champaign.

REFERENCES

Bluestein, H. B., and M. H. Jain, 1985: Formation of mesoscale lines of precipitation: Severe squall lines in Oklahoma during spring. *J. Atmos. Sci.*, **42**, 1711–1732.

Browning, K. A., 1977: The structure and mechanism of hailstorms. *Meteor. Monogr.*, No. 38, Amer. Meteor. Soc., 1–39.

Chalon, J.-P., J. C. Fankhauser and P. J. Eccles, 1976: Structure of an evolving hailstorm. Part I: General characteristics and cellular structure. *Mon. Wea. Rev.*, **104**, 564–575.

Chong, M., P. Amayenc, G. Scialom and J. Testud, 1987: A tropical squall line observed during the COPT 81 experiment in West Africa. Part I: Kinematic structure inferred from dual-Doppler radar data. *Mon. Wea. Rev.*, **115**, 670–694.

Clark, T. L., 1979: Numerical simulations with a three-dimensional cloud model: Lateral boundary condition experiments and multicellular severe storm simulations. *J. Atmos. Sci.*, **36**, 2191–2215.

Cotton, W. R., M. A. Stephens, T. Nehrkorn and G. J. Tripoli, 1982: The Colorado State University three-dimensional cloud/mesoscale model—1982. Part II: An ice phase parameterization. *J. Rech. Atmos.*, **16**, 295–320.

——, G. J. Tripoli, R. M. Rauber and E. A. Mulvihill, 1986: Numerical simulation of the effects of varying ice crystal nucleation

rates and aggregation processes on orographic snowfall. *J. Climate Appl. Meteor.*, **25**, 1658–1680.

Droegemeier, K. K., and R. B. Wilhelmson, 1987: Numerical simulation of thunderstorm outflow dynamics. Part I: Outflow sensitivity experiments and turbulence dynamics. *J. Atmos. Sci.*, **44**, 1180–1210.

Dudhia, J., M. W. Moncrieff and D. W. K. So, 1987: The two-dimensional dynamics of West African squall lines. *Quart. J. R. Met. Soc.*, **113**, 121–146.

Dye, J. E., C. A. Knight, V. Toutenhoofd and T. W. Cannon, 1974: The mechanism of precipitation formation in Northeastern Colorado cumulus III. Coordinated microphysical and radar observations and summary. *J. Atmos. Sci.*, **31**, 2152–2159.

Fankhauser, J. C., 1982: The 22 June 1976 case study: Large-scale influences, radar echo structure, and mesoscale circulations. *Hailstorms of the Central High Plains, Vol. 2*, Colorado Associated University Press, 1–34.

Feteris, P. J., 1961: The influence of the circulation around cumulonimbus clouds on the surface humidity pattern. *Swiss Aero-Rev.*, **36**(11), 626–630.

Foote, G. B., and C. G. Wade, 1982: Case study of a hailstorm in Colorado. Part I: Radar echo structure and evolution. *J. Atmos. Sci.*, **39**, 2828–2846.

——, and H. W. Frank, 1983: Case study of a hailstorm in Colorado. Part III: Airflow from triple-Doppler measurements. *J. Atmos. Sci.*, **40**, 686–707.

Gamache, J. F., and R. A. Houze, Jr., 1982: Mesoscale air motions associated with a tropical squall line. *Mon. Wea. Rev.*, **110**, 118–135.

——, and ——, 1983: Water budget of a mesoscale convective system in the tropics. *J. Atmos. Sci.*, **40**, 1835–1850.

——, and ——, 1985: Further analysis of the composite wind and thermodynamic structure of the 12 September GATE squall line. *Mon. Wea. Rev.*, **113**, 1241–1259.

Heymsfield, G. M., and S. Schotz, 1985: Structure and evolution of a severe squall line over Oklahoma. *Mon. Wea. Rev.*, **113**, 1563–1589.

Houze, R. A., Jr., 1977: Structure and dynamics of a tropical squall-line system. *Mon. Wea. Rev.*, **105**, 1540–1567.

Klemp, J. B., and R. B. Wilhelmson, 1978: The simulation of three-dimensional convective storm dynamics. *J. Atmos. Sci.*, **35**, 1070–1096.

——, R. Rotunno and M. L. Weisman, 1985: Numerical simulations of squall lines in two and three dimensions. Preprints, *14th Conf. Severe Local Storms*, Indianapolis, Amer. Meteor. Soc., 179–182.

Knight, C. A., W. A. Cooper, D. W. Breed, I. R. Paluch, P. L. Smith and G. Vali, 1982: Microphysics. *Hailstorms of the Central High Plains, Vol. 1*, Colorado Associated University Press, 151–193.

Leary, C. A., and R. A. Houze, Jr., 1979: The structure and evolution of convection in a tropical cloud cluster. *J. Atmos. Sci.*, **36**, 437–457.

LeMone, M. A., 1983: Momentum transport by a line of cumulonimbus. *J. Atmos. Sci.*, **40**, 1815–1834.

——, G. M. Barnes and E. J. Zipser, 1984: Momentum flux by lines of cumulonimbus over the tropical oceans. *J. Atmos. Sci.*, **41**, 1914–1932.

Lin, Y.-L., R. D. Farley and H. D. Orville, 1983: Bulk parameterization of the snow field in a cloud model. *J. Climate Appl. Meteor.*, **22**, 1065–1092.

Lord, S. J., H. E. Willoughby and J. M. Piotrowicz, 1984: Role of a parameterized ice-phase microphysics in an axisymmetric, nonhydrostatic tropical cyclone model. *J. Atmos. Sci.*, **41**, 2836–2848.

Marshall, J. S., and W. McK. Palmer, 1948: The distribution of raindrops with size. *J. Meteor.*, **5**, 165–166.

Miller, M. J., 1978: The Hampstead storm: A numerical simulation of a quasi-stationary cumulonimbus system. *Quart. J. R. Met. Soc.*, **104**, 413–427.

Newton, C. W., 1950: Structure and mechanism of the prefrontal squall line. *J. Meteor.*, **7**, 210–222.

——, 1966: Circulations in large sheared cumulonimbus. *Tellus*, **18**, 699–712.

Nicholls, M. E., 1987: A comparison of the results of a two-dimensional numerical simulation of a tropical squall line with observations. *Mon. Wea. Rev.*, **115**, 3055–3077.

Ogura, Y., and N. A. Phillips, 1962: Scale analysis of deep and shallow convection in the atmosphere. *J. Atmos. Sci.*, **19**, 173–179.

——, and M.-T. Liou, 1980: The structure of a midlatitude squall line. *J. Atmos. Sci.*, **37**, 553–567.

Rotunno, R., J. B. Klemp and M. L. Weisman, 1988: A theory for strong, long lived squall lines. *J. Atmos. Sci.*, **45**, 463–485.

Roux, F., J. Testud, M. Payen and B. Pinty, 1984: West African squall-line thermodynamic structure retrieved from dual-doppler radar observations. *J. Atmos. Sci.*, **41**, 3104–3121.

Rutledge, S. A., 1986: A diagnostic modeling study of the stratiform region associated with a tropical squall line. *J. Atmos. Sci.*, **43**, 1356–1377.

——, and P. V. Hobbs, 1983: The mesoscale and microscale structure and organization of clouds and precipitation in midlatitude cyclones. Part VIII: A model for the "seeder-feeder" process in warm frontal rainbands. *J. Atmos. Sci.*, **40**, 1185–1206.

Sanders, F., and K. A. Emanuel, 1977: The momentum budget and temporal evolution of a mesoscale convective system. *J. Atmos. Sci.*, **34**, 322–330.

Schmid, W., and A. Waldvogel, 1986: Radar hail profiles in Switzerland. *J. Climate Appl. Meteor.*, **25**, 1002–1011.

Smull, B. F., and R. A. Houze, Jr., 1985: A midlatitude squall line with a trailing region of stratiform rain: Radar and satellite observations. *Mon. Wea. Rev.*, **113**, 117–133.

——, and ——, 1987a: Dual-doppler analysis of a midlatitude squall line with a trailing region of stratiform rain. *J. Atmos. Sci.*, **44**, 2128–2148.

——, and ——, 1987b: Rear inflow in squall lines with trailing stratiform precipitation. *Mon. Wea. Rev.*, **115**, 2869–2889.

Soong, S.-T., and Y. Ogura, 1980: Response of tradewind cumuli to large-scale processes. *J. Atmos. Sci.*, **37**, 2035–2050.

——, and W.-K. Tao, 1984: A numerical study of the vertical transport of momentum in a tropical rainband. *J. Atmos. Sci.*, **41**, 1049–1061.

Stewart, R. E., J. D. Marwitz, J. C. Pace and R. E. Carbone, 1984: Characteristics through the melting layer of stratiform clouds. *J. Atmos. Sci.*, **41**, 3227–3237.

Thorpe, A. J., M. J. Miller and M. W. Moncrieff, 1982: Two-dimensional convection in non-constant shear: A model of mid-latitude squall lines. *Quart. J. R. Met. Soc.*, **108**, 739–762.

Wade, C. G., and G. B. Foote, 1982: The 22 July 1976 case study: Low level airflow and mesoscale influences. *Hailstorms of the Central High Plains, Vol. 2*, Colorado Associated University Press, 115–130.

Wakimoto, R. M., 1982: The life cycle of thunderstorm gust fronts as viewed with Doppler radar and rawinsonde data. *Mon. Wea. Rev.*, **110**, 1060–1082.

Weisman, M. L., and J. B. Klemp, 1982: The dependence of numerically simulated convective storms on vertical wind shear and buoyancy. *Mon. Wea. Rev.*, **110**, 504–520.

Wilhelmson, R. B., and Y. Ogura, 1972: The pressure perturbation and the numerical modeling of a cloud. *J. Atmos. Sci.*, **29**, 1295–1307.

Yoshizaki, M., 1986: Numerical simulations of tropical squall-line clusters: Two-dimensional model. *J. Meteor. Soc. Japan*, **64**, 469–491.

Zipser, E. J., 1969: The role of organized unsaturated convective downdrafts in the structure and rapid decay of an equatorial disturbance. *J. Appl. Meteor.*, **8**, 799–814.

——, 1977: Mesoscale and convective-scale downdrafts as distinct components of squall-line structure. *Mon. Wea. Rev.*, **105**, 1568–1589.